UPPSALA
UNIVERSITET

UPTEC F 24030

Examensarbete 30 hp

Juni 2024

Diffusion of volatile fission products in very heavy reactor fuel matrices

Nils Wikström

Civilingenjörsprogrammet i teknisk fysik

UPPSALA
UNIVERSITET

Diffusion of volatile fission products in very heavy reactor fuel matrices

Nils Wikström

Abstract

The interplay of nuclear fuel with fission products is key for safe and efficient nuclear power operation. The diffusion of volatile fission products in very heavy reactor fuel matrices was investigated by analysing Zirconium Dioxide and Uranium Nitride, implanted with different ions. The samples were implanted using the 350kV Ion Implanter available at Uppsala University. Zirconium Dioxide was implanted with Xenon, Krypton and Iron, and Uranium Nitride was implanted with Krypton and Zirconium. The samples were then analysed using Time of Flight Elastic Recoil Detection Analysis (ToF-ERDA), Rutherford Backscattering Spectrometry (RBS), Scanning Electron Microscopy (SEM), and X-Ray Diffraction (XRD). After the implantation and analysis, the samples were annealed at different times and temperatures. The annealing times were predicted by solving Fick's second law with numerical methods and using Stopping and Range of Ions in Matter (SRIM) as an initial guess. The results show that annealing times can be predicted by solving Fick's second law, to first order, and that ion implantation effects the stoichiometry of the samples. Future improvements could include improvement of underlying physics in the annealing predictions, and more extensive measurements performed on a wider range of samples.

Teknisk-naturvetenskapliga fakulteten

Uppsala universitet, Utgivningsort: Uppsala/Visby

Handledare: Robert Frost Ämnesgranskare: Daniel Primetzhofer

Examinator: Tomas Nyberg

Populärvetenskaplig sammanfattning

Kärnkraft är en viktig energikälla som använder olika kärnbränslen för att generera elektricitet. När dessa bränslen genomgår fission, produceras olika ämnen såsom xenon, krypton och zirkonium. Dessa ämnen påverkar kärnbränslets egenskaper, vilket gör det viktigt att förstå hur dessa ämnen beter sig i kärnbränslet. Syftet med projektet var att studera hur dessa ämnen sprider sig i kärnbränslen. Prover av Zirkoniumdioxid och Uraniumnitrid implanterades med olika joner och analyserades med jonstråletekniker. Dagens metoder använder aktivt kärnbränsle för att studera detta, men i detta projekt föreslogs en metod som använder naturligt kärnbränsle istället. Denna metod visade sig fungera mycket bra för att studera spridningen av de intressanta ämnerna.
Resultaten visade att spridningen av jonerna kan förutsägas och att implantationen ändrar materialens sammansättning. Det upptäcktes att gasformiga ämnen är svårare att implantera i bränslet än fasta ämnen på grund av effekter som bakåtspridande, sputtring och flyktighet hos gasformiga ämnen. Genom att förstå hur dessa ämnen rör sig och påverkar kärnbränslet kan vi förbättra säkerheten och effektiviteten i framtida kärnreaktorer. Denna forskning bistår med att utveckla bättre och säkrare kärnenergi.

Contents

List of Figures

List of Tables

List of Abbreviations

at. %	Atomic Percent
CC	Calculated Concentration
dpa	displacements per atom
EDS	Energy Dispersive X-ray Spectrometry
MCI	Medium Current Implanter
PKA	Primary Knock on Atom
ppm	Parts Per Million
ppt	Parts Per Thousand
RBS	Rutherford Backscattering Spectrometry
SEM	Scanning Electron Microscopy
TC	Theoretical concentration
TOF-ERDA	Time of Flight Elastic Recoil Detection Analysis
XRD	X-ray Diffraction

Chapter 1

Introduction

Nuclear energy is a valuable source of electricity and energy. As nuclear fuels, such as Uranium Dioxide (UO_2) or Uranium Nitride (UN) undergo fission they release fission products such as xenon (Xe), krypton (Kr), zirconium (Zr) or barium (Ba). The fission products alter the thermal and structural properties of the fuel which is important to understand for safe nuclear fuel operation. The goal of this project was to analyze the mechanisms of the fission products diffusion process.

As these fission products diffuse in the fuel's structure, the composition, properties, and stability of the nuclear fuel is affected, therefore it is important to know the interplay between the produced fission products and the nuclear fuel. By gaining insight into the diffusion mechanism of volatile fission products, the project aims to give knowledge to improve reactor design, safety, and fuel management.

1.1 Background and Motivations

The diffusion of gaseous and solid fission products such as Xe, Kr, and Zr in nuclear fuel alters the properties of nuclear fuel and is key to understand for safe reactor operation. Studying the diffusion of volatile fission products in nuclear fuel is challenging since problems surface when implanting gases into the fuel matrix and when finding techniques that can analyze the concentration of the fission products at short length scales. To study the diffusion in nuclear fuel, such as Uranium dioxide, the diffusion parameters have been approximated from irradiated and activated nuclear fuel or from gas release after annealing of fuel samples. The methods above experience problems from the fact that bulk- and grain-boundary thermal and athermal diffusion is highly approximated in the fuel. This leads to diffusion parameters that have a large spread, and the understanding of this is key for safe nuclear fuel operation. Using irradiated materials requires advanced and expensive equipment as well as samples that are characterized thoroughly. The expensive equipment and use of irradiated fuel make current methods costly and limit the number of samples that can be analyzed [1][2].

The mobility of the fission products is highly dependent on the solubility of the fission products in the fuel matrix. When heated by fuel operation, fission products distribute dynamically in the lattice and precipitate into inter- and intragranular bubbles. The release of short-lived fission gases has been extensively studied in several experiments and generally shows that diffusion of fission products is the rate-determining mechanism in the release of volatile fission products. An increase or decrease in the stoichiometry of primary atoms in the fuel causes the thermal capabilities of the fuel to change and is therefore important to understand for the operation of nuclear reactors [2][3].

Developing a new method that uses unirradiated fuel and analyzing the diffusion of ion-implanted fission products with Ion Beam Analysis techniques such as Time of flight recoil detection analysis (ToF-ERDA) to provide depth profiles as proposed by Frost et al. is therefore highly motivated. Using ToF-ERDA, thereafter annealing and re-analyzing the depth profiles does not require any irradiated samples and is therefore safer to use. The method, when fully developed, will provide many uses in the development of Generation IV reactors [1].

1.2 Project Goals

The goal of this project was to optimize the workflow suggested by Frost et al. This was done by predicting annealing times through numerical methods and by conducting extensive measurements using different ions at different energies. In the project, two types of samples were to be implanted and annealed. The sample matrices were Zirconium Dioxide (ZrO_2), used as a surrogate for UO_2, and UN [1].

The key objectives of the project were:

1. implantation of volatile elements in a range of heavy sample matrices, using the ion implanter at the Tandem laboratory;
2. assessment of the implantations with ToF-ERDA, using the 5 MV accelerator at the Tandem Laboratory;
3. perform sample annealing at a range of temperatures and temperature gradients;
4. repeat ToF-ERDA measurements to evaluate the thermally-induced diffusion of the implanted ions;
5. derive first order approximations of annealing times in heavy sample matrices.

1.3 Structure of this Thesis

This Thesis is divided into six main chapters. These are Introduction, Theory, Methodology, Results, Discussion, and Conclusions and Outlook. Chapter 1 aims to give the reader a good understanding of the project goals and motivates the experiments performed in the project. In Chapter 2, basic concepts needed to understand the different methods used in the project as well as the underlying physics are presented. There are also theoretical explanations of each analysis technique used during the project. Moreover, in Chapter 3, the reader is introduced to the process used on all samples and then an individual assessment of the analysis made on each sample in the thesis is presented. An overview of the equipment and analysis techniques used is also given including the simulation process that was created during the project. In Chapter 4, all results from the different measurements performed and calculations made are presented in figures and tables. Each unique sample in the thesis is structured in its own section. Furthermore, in Chapter 5, the results are analyzed thoroughly in five different sections. The first section aims to explain the study of diffusion of volatile fission products that were made in the Zirconium

Dioxide samples. The second section explains the effects of oxidation that were present post-implantation of ions in the Uranium Nitride matrix. The third section evaluates the effects on the stoichiometry of Uranium Nitride as ions were implanted. The fourth section evaluates why different ions were implanted with different concentrations, as compared to theoretical data from SRIM. The last section aims to explain the limitations of the ToF-ERDA measurements performed in the project. Finally, Chapter 6, summarizes key findings in the project and suggests future work that could be conducted building on this thesis.

Chapter 2

Theory

In this chapter, different fundamental concepts will be introduced. The theory will introduce some basic concepts needed to understand the thesis and apply the concepts presented to different methods used in the project.

2.1 Binary collisions

When an energetic ion travels through a solid, it interacts with the atoms of the solid by colliding with them. This can generally be modeled as a binary collision, meaning a collision between two bodies [4].

In an elastic collision, the energy and momenta are conserved, and from those conserved quantities, we can derive an important factor that is needed for Ion Beam Analysis(IBA), the kinematic factor. The kinematic factor relates the energy of the incident ion to the recoiled atom or itself after the collision. The experimental setup in the laboratory frame is depicted in Figure 2.1 [5].

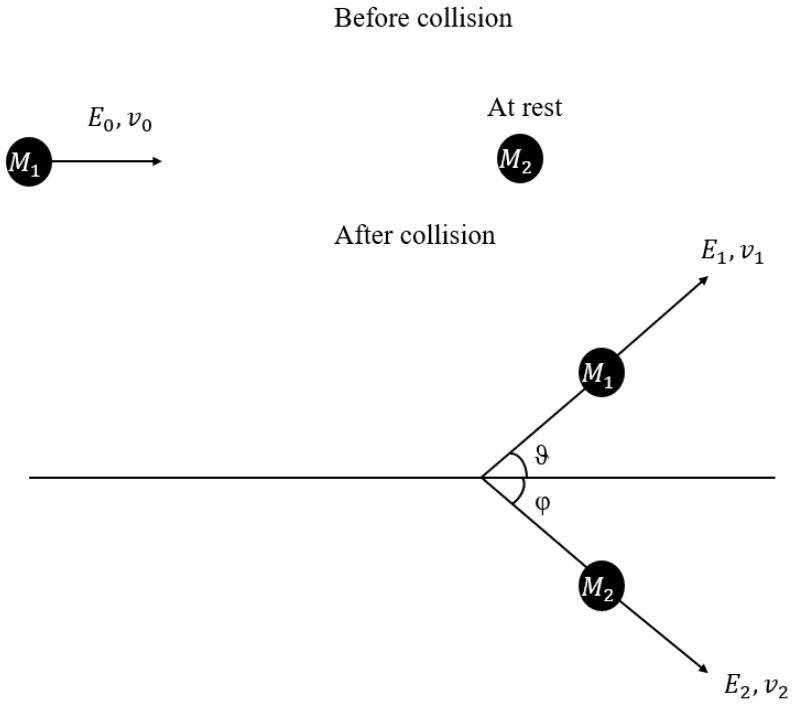

Figure 2.1: Schematic of elastic collision of two particles, one is at rest in the initial state.

From Figure 2.1 we have

$$E_0 = \frac{m_1 v_0^2}{2} = \frac{m_1 v_1^2}{2} + \frac{m_2 v_2^2}{2} = E_1 + E_2 \tag{2.1}$$

$$m_1 v_0 = m_1 v_1 \cos(\theta) + m_2 v_2 \cos(\theta) \tag{2.2}$$

$$0 = m_1 v_1 \sin(\theta) - m_2 v_2 \sin(\theta), \tag{2.3}$$

with m_1 being the mass of the incident particle, v_0 being the velocity of the incident particle before collision, v_1 being the velocity of the incident particle after collision, m_2 being the mass of the recoiling particle, v_2 being the velocity of the recoiling particle, E_0 being the energy of the incident particle before collision, E_1 being the energy of the incident particle after collision, E_2 being the energy of the recoiling atom after collision, and θ being the scattering angle of the incident particle.

This system of equations can be solved for E_1 as a function of E_0, which leads to

$$E_1 = E_0 \left[\frac{(m_2^2 - m_1^2 \sin^2(\theta))^{1/2} + m_1 \cos(\theta)}{m_2 + m_1} \right]^2 = \gamma E_0, \tag{2.4}$$

with γ being the kinematic factor and ϕ being the scattering angle of the particle initially at rest. We can also choose to eliminate E_1 from the system of equations above, in which we find

$$E_2 = E_0 \frac{4 m_1 m_2}{(m_1 + m_2)^2} \cos^2 \phi, \tag{2.5}$$

where ϕ is the scattering angle of the recoiling particle. This expression is necessary to find the maximum transferred energy, which trivially is when $\phi = 0$ [6].

2.2 Scattering cross sections

In ion-solid interactions, the number of particles scattered by the polar angle θ is what is known as the scattering cross section. The cross section has units of area, and a common unit to use is barn (1 barn = 10^{-24}cm^2). It should be seen as an effective area that is seen by an incident particle that is interacting with the target [7].

For highly energetic ions, the scattering cross section is well described by the Rutherford cross section. This is defined as

$$\left(\frac{\partial \sigma}{\partial \Omega} \right)_{Rutherford} = \left(\frac{Z_1 Z_2 e^2}{8 \pi \varepsilon_0 E} \right)^2 \frac{1}{\sin^4(\theta/2)}, \tag{2.6}$$

where Z_1 is the atomic number of the incident particle, Z_2 is the atomic number of the scattered particle, E is the energy of the system, e is the elementary charge, ε_0 is the permittivity in

vacuum and θ is the scattering angle. In the laboratory frame, the Rutherford cross section is defined as

$$\left(\frac{\partial\sigma}{\partial\Omega}\right)_{Lab} = \left(\frac{Z_1 Z_2 e^2}{8\pi\epsilon_0 E}\right)^2 \frac{1}{\sin^4(\theta)} \frac{\left((1-(M_1/M_2\sin\theta)^2)^{1/2}+\cos\theta\right)^2}{(1-(M_1/M_2\sin\theta)^2)^{1/2}} \tag{2.7}$$

where M_1 is the mass of the incident particle, E_1 is the energy of the incident particle, M_2 is the mass of the target, and the remaining quantities are defined as in equation (2.6)[7].

2.3 Stopping power

When energetic ions penetrate a target they undergo several interactions with the target's nucleus and electrons which makes the ions lose energy. The rate at which the incident ions lose energy is called the stopping power of the material and is dependent on the incident ion's energy, mass, and atomic number as well as on the mass, atomic number, and density of the target. After several collisions, the ion will be at rest in the material. We call the average distance traveled into the material the range, R, of the ions and it is defined by

$$R = \int_{E_0}^{0} \left(\frac{dE}{dx}\right)^{-1} dE, \tag{2.8}$$

where R $\frac{dE}{dx}$ is the stopping power and E_0 is the incident energy. The sign of the stopping power is negative since it represents the loss of energy in the solid [8].

The stopping power is determined by two different interactions. The first is the collisions with the nucleus of the material, where energy is transferred to the target nuclei by elastic collisions, and the second is the interactions with the electrons of the target, where energy is lost due to ejections or excitations of atomic electrons. Therefore we can express the stopping power as

$$\frac{dE}{dx} = \left.\frac{dE}{dx}\right|_n + \left.\frac{dE}{dx}\right|_e, \tag{2.9}$$

where subscripts n and e represent nuclear and electronic stopping powers. For high energies with a light ion, the electronic interaction dominates. For low energies with heavy ions, the nuclear interaction dominates. The nuclear stopping power is very small at energies above 200 keV/amu and is often disregarded in calculations due to this. It is typically below 1% of the electronic stopping power and hence the electronic stopping power typically determines the stopping of ions in a solid [8][9].

The electronic stopping power can be expressed as

$$-\left.\frac{dE}{dx}\right|_e = \int I(v,\rho)[Z_1^*(v)]^2 \rho dV, \tag{2.10}$$

where I is the stopping interaction function of a particle with velocity, v, and electron gas density ρ, Z_1^* is the effective charge of an ion with atomic number Z_1 and the integral is over each volume

element of the target. It is important to note that the electronic stopping power scales with the square of the incident ions mass [9].

The stopping power in compounds is approximated using Bragg's rule. It states that the stopping power in a compound is equal to the sum of the stopping powers of each element in the compound. Bragg's rule is defined as

$$-\frac{dE_{tot}}{dx} = \sum_x r_x \frac{dE_x}{dx}, \tag{2.11}$$

where r_x is the ratio of number density of the atom x to the total number density in the compound, $\frac{dE_x}{dx}$ is the stopping power in the material for atom x and $\frac{dE_{tot}}{dx}$ is the total stopping power [10].

To calculate ranges from stopping powers there are different softwares and stopping power data collections such as Stopping and Ranges of Ions in Matter (SRIM). These softwares are all based on different models of the stopping power, which leads to different strengths and weaknesses. For instance, SRIM does not account for channeling and calculates the stopping power of compounds with Bragg's rule [11].

2.3.1 Radiation damage

Lattice atoms struck by energetic ions must receive a minimum amount of energy to be displaced from their lattice site. This energy is called the displacement energy, E_d. If the collision transfers less energy than E_d, the energy is released as phonons. If the energy is greater than the displacement energy, the atom will leave its lattice site and create a vacancy. This atom can then occupy an interstitial site in the lattice and the vacancy-interstitial pair is called a Frenkel pair. The displacement energy is typically around 100 eV [12].

If the energy of the incident ion is much larger than E_d, the primary knock-on atom (PKA) can continue the collision process and create a displacement cascade, as the atom interacts with other atoms in the lattice. If the energy given from the PKA to the next lattice atom is greater than E_d but less than $2E_d$ the struck atom leaves its lattice site but the lattice site is then occupied by the PKA. The process of creating a vacancy that is instantly occupied by the PKA is called a replacement collision. If the energy of the PKA is greater than $2E_d$, the PKA creates displacement cascades, with the number of displacements proportional to the energy. A common measure for irradiation damage is displacements per atom (dpa). One unit of dpa means that on average, every atom has been displaced one time from its stable lattice point in a selected volume [12].

In nuclear fuels, the type of damage source creates different effects of radiation damage. One of the sources of radiation damage in nuclear fuel is atomic displacements mainly caused by the fission processes in the material. Most of the energy of the fission products in the fuel is lost due to the electronic stopping power as explained in Section 2.3. The energy lost to the nuclear fuel matrix then ionizes and excites electrons in the lattice and the energy released can cause more radiation damage in the fuel. In nuclear fuel the radiation damage effects are complex due to the different sublattices present in ceramics such as UO_2 and UN. The diffusion of gaseous fission products in UO_2 is complex and is not governed by one diffusion rate [13][14].

As uranium (U) based fuels undergo fission they form fission products in the lattice. Some of

these are inert gases such as Kr and Xe. The gases are insoluble in the matrix and form gas bubbles. The gas bubbles are affected by forces from temperature gradients and generally move up the gradients. The gas bubbles cause the nuclear fuel to swell since there are bubbles of accumulated fission products and is important to understand in the operation of nuclear reactors as the swelling can cause cracking of the fuel pellets. The formation of gas bubbles and clusters of fission products is largely governed by the temperature. As the fuel reaches a high burnup structure, fission gas is released from the matrix and the damage induced in the sample is reduced greatly. The fission products can also be trapped during formation or along their diffusion paths by radiation-induced defects and small vacancy clusters [15] [16] [17].

2.3.2 Range distributions and straggling

The stopping of an ion in a solid is a stochastic process. Every ion has a different stopping sequence, and the range of an ion in the solid will vary from ion to ion. The depth distribution is typically in the shape of a Gaussian, and the standard deviation is called the range straggling. Straggling can also occur in the energy domain. At a given range the energies are different since each ion has interacted with an individual amount of atoms. This phenomenon is called energy straggling and gives us a broader energy spectrum at a given depth [18].

Many materials show crystalline structures and the structure affects the ion's interaction with the material. In single-crystal substrates, the orientation of the crystal has a large effect on the range distribution. The orientation of the crystals influence on the range is called channeling, and means that there are orientations in a crystalline material where there is a lower chance of colliding with an atom [19].

2.4 Ion Implantation

An ion implanter generally consists of an ion source, an electrostatic extraction field, an acceleration system, an analyzing system, and a scanning system. A typical example of an ion implanter is a medium current implanter (MCI), which gives currents up to 3 mA and energies of 100 - 500 keV. An MCI generally works by first creating a plasma from the given ion source, accelerating it, and selecting the wanted ions with an analyzing magnet. The selected ions are then accelerated again to the selected energy and thereafter directed on the implantation target [20].

Generally, the ion source is created by a cathode and an anode. The cathode is heated and supplies electrons that will ionize the gas. The anode helps in ionizing the gas and provides the initial acceleration since a voltage between the cathode and the anode is applied. In the chamber, the pressure is kept very low to stop discharges from happening [20].

When a discharge is created between the cathode and anode, the ions need to be extracted from the plasma. The beam can be extracted from an aperture in the electrodes. Most ion implanters use a magnetic field to influence the path of the created ions. The beam is formed and extracted by applying an electric field between the ion source and the electrode with the aperture. The beam can then pass through the electrode, and therefore be extracted [20].

Further, the quality of the beam needs to be checked and modified. The quality of the beam

is primarily governed by the shape of the plasma surface and the current density inside this surface. The current density inside of the plasma surface is called the emittance of the beam and is defined as the area occupied by the beam in position and momentum space. It is also important to control the energy spread and the current modulation of the beam, and it is usually performed with help from an analyzing magnet. The magnet generally bends the beam through 90°and analyses the masses passing through this curve. Due to the Lorentz force, the acceleration in the curve is proportional to the inverse of the mass and yields an opportunity to select a specific mass of the beam. When the selected ions are separated from the other present ions, they are once again accelerated. The ion beam is directed towards the target that is to be implanted with ions. When the ions hit the target they penetrate it and experience a stopping power according to equation 2.9. When the ions have no energy left, they stop and are therefore implanted [20].

2.5 Diffusion

Transport and diffusion in materials are governed by Fick's Laws. Diffusion is defined as the movement of a substance from a high-concentration region to a lower-concentration region. Fick's laws state that the diffusion is proportional to the negative of the concentration gradient, with a proportionality constant D, which is called the diffusion coefficient. Diffusion can also occur when there is a pressure or temperature gradient. Fick's first law is given by

$$J = -D\frac{\partial c}{\partial x}, \tag{2.12}$$

where J is the rate of transfer per unit area, D is the diffusion coefficient [m^2 s^{-1}], and c is the concentration. Fick's second law can from Equation (2.12) be derived and is formulated as

$$\frac{\partial c}{\partial t} = D\frac{\partial^2 c}{\partial x^2}, \tag{2.13}$$

where we have defined c and D as above. Fick's second law governs how the concentration of a substance in a solid evolves over time [21].

There are many different types of diffusion mechanisms. The most common mechanisms are the vacancy mechanism, direct interstitial mechanism, and the Interstitialcy mechanism. Another important mechanism is grain boundary diffusion, as well as self-diffusion. For nuclear fuel, the mechanism dominating can be different depending on the fuel. The diffusion in nuclear fuel is dependant on the stoichiometry of the material [21][22][23][24].

The incident radiation on a material creates point defects and vacancies and causes diffusion of atoms in the solid. This type of diffusion is called radiation-enhanced diffusion. Radiation-enhanced diffusion can, if present, be dominant over all other diffusion mechanisms, is temperature dependent, and can be several orders of magnitude greater than the thermal diffusion coefficient. The high diffusion coefficient for radiation-enhanced diffusion cannot be explained by regular collision cascades or thermal diffusion, but must be the cause of vacancies formed due to irradiation and fission [24][25][26].

2.5.1 Arrhenius equation

Generally, the variation of the diffusion coefficient with pressure is less prevalent than the variation with temperature. Therefore, it is necessary to model the diffusion coefficient with temperature. The temperature dependence of the diffusion coefficient is well described by the Arrhenius equation. The Arrhenius equation is stated as

$$D = D_0 \exp\left(-\frac{E_a}{k_b T}\right), \tag{2.14}$$

where D_0 is the pre-exponential factor, E_a is the activation energy for diffusion, k_b is the Boltzmann constant and T is the temperature. D_0 is sometimes called the frequency factor [27].

2.6 ToF-ERDA

ToF-ERDA is based on the elastic scattering of incident ions with the nucleus of the target. A typical experimental setup for ToF ERDA is given in figure 2.2[28].

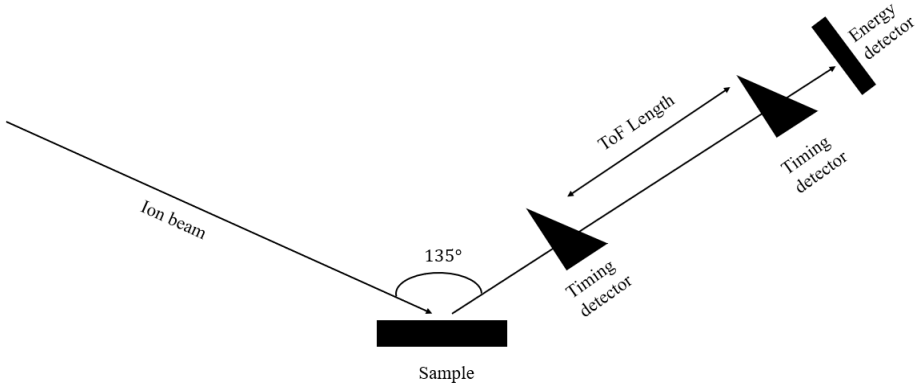

Figure 2.2: Schematic representation of a ToF ERDA set up.

In ToF ERDA the measured quantity is the energy of the recoiling nucleus, as well as the time of flight between the two detectors. From these two values, the mass of the recoiled ion can be calculated by the kinetic energy- velocity relation.

$$E_k = \frac{mv^2}{2} = \frac{ml^2}{2t^2} \iff m = \frac{2E_k t^2}{l^2}, \tag{2.15}$$

where E_k is the measured kinetic energy, m is the mass of the recoiled atom, l is the flight length and t is the time of flight. The measurements will yield hyperbolic-shaped curves since the two quantities have a hyperbolic relation. An example is given in Figure 2.3. Prior knowledge of the sample is needed to understand which curve corresponds to which element. The example in Figure 2.3, was a Kr implanted ZrO_2 stick, with the presence of carbon (C), oxygen (O), aluminium (Al), hafnium (Hf) and gold (Au), and chromium (Cr) [28].

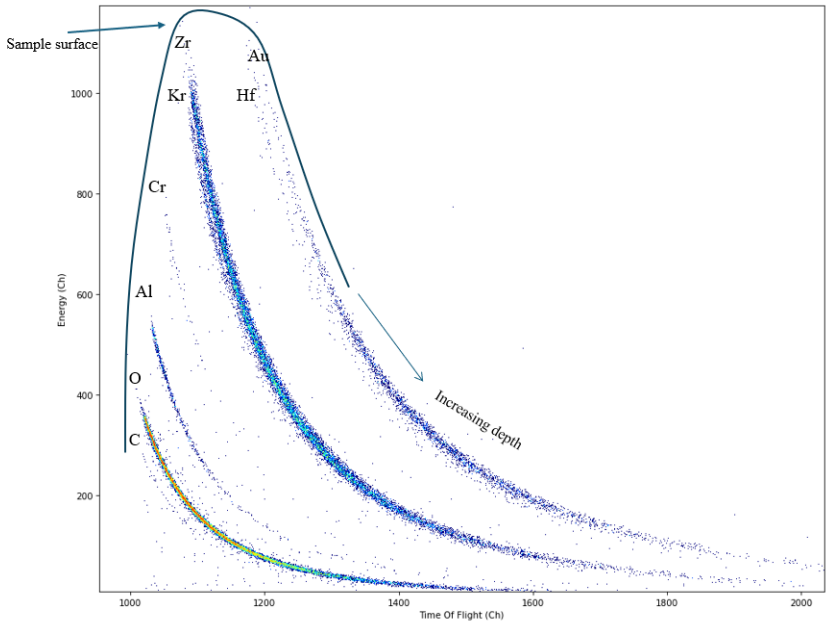

Figure 2.3: An example of output data from a typical ToF-ERDA measurement with the sample surface and increasing depth marked.

ToF-ERDA is best suited for the analysis elements with a heavy ion beam. The use of a heavy ion beam limits the penetration depth and is only applicable at ranges of a few microns. The method is very successful in analyzing depth profiles. It is non-destructive, features many different elements, is very sensitive, and has great depth resolution [28] [29].

ToF-ERDA is advantageous to use since it is a quantitative method if only Coulomb scattering can be assumed. Heavy ions of 1-2 MeV/u satisfy this condition. For heavy projectiles and light targets the Rutherford cross section defined in equation (2.7), can be approximately made independent of the target atom, since $M_1 >> M_2$. Therefore, light elements can be detected with equal sensitivity in ToF-ERDA. When dealing with heavier targets, the statement does not hold, and the scattering cross section will be dependent on the target. The increased scattering cross section makes most scatterings favor the heavier elements in a ToF-ERDA measurement and causes effects from multiple and plural scattering to arise. As heavier elements have greater energy losses as seen in Equation (2.10), they are more challenging to detect. The multiple- and plural scattering can also introduce tails in the elemental energy depth profiles [29][30].

Data from ToF-ERDA measurements is often analyzed with software such as Potku, or CONTES. The calculation of the depth profiles in the software is produced by an iterative process, where the yield is compared to the stopping power of the element[31] [32][33].

2.7 Rutherford backscattering spectrometry

Rutherford backscattering spectrometry (RBS) measures the energies of the backscattered ions from the target. The incident ion beam is usually helium ions with energies in the MeV range. Helium is often used due to its light mass and inert properties. Since backscattering can only occur between elements heavier than the incident ion, helium is often used since it allows detection of all elements with atomic number $Z > Z_{He}$. The energies of the backscattered

helium ions are compared to the conservation of energy and momenta and can relate the energy to the depth and mass of the target. The number of backscattered ions from a given element is proportional to its concentration, and because of this, RBS can quantitatively define the depth profile of elements in a solid if the stopping power is known. The spectrum of RBS hence depends both on the depth and mass of the element of which the incident ion backscatters from [28].

2.8 Scanning electron microscopy

Scanning electron microscopy (SEM) is a method used to observe the surface layer of a specimen. The sample in SEM is irradiated with electrons from an electron gun. From the irradiation, the sample can either emit backscattered electrons or secondary electrons. The backscattered electrons are electrons that simply scatter back off from the sample and the secondary electrons are electrons emitted from the surface atoms due to the energy transmitted from the primary electrons [34].

A typical SEM is built from four different parts. These are an electron gun, a condensor lens, a scanning lens, and an electron detector. The electron gun supplies the electrons, usually through the thermal emission of a cathode like tungsten. The condensor lens is used to do an initial adjustment of the electron beam, and the focusing lens is used to focus the electron beam onto the specimen, and to determine the working distance of the microscope [34].

A common analysis method using SEM is Energy Dispersive X-ray Spectrometry (EDS) in which all elements from beryllium to U can be detected. EDS makes use of the characteristic X-rays emitted from elements, by exciting the electrons in the atom. Since the X-rays correspond to a specific element, a compositional analysis can be made using EDS [35].

2.9 X-ray diffraction

X-ray diffraction (XRD) is a common method used to investigate structural properties of materials. The output signal is the result of elastic scattering of monochromatic X-rays in core electrons of atoms in a sample. Since the atoms generally form in a lattice structure, the crystal lattice causes the X-rays to be diffracted and creates well-known diffraction patterns. From the signal, both structural and compositional data can be extracted by deriving miller indices from the distances between lattice layers [36].

Chapter 3

Methodology

This chapter explains the experimental set-ups used in the project and outlines the methodology. Motivations for used ion beams, materials, and techniques are also given.

3.1 Process overview

This thesis was conducted following the methodology proposed by Frost et al. This method, as described in Chapter 1, was used throughout the project and is described in more detail below [1]. An illustration of the methodology is shown in Figure 3.1.

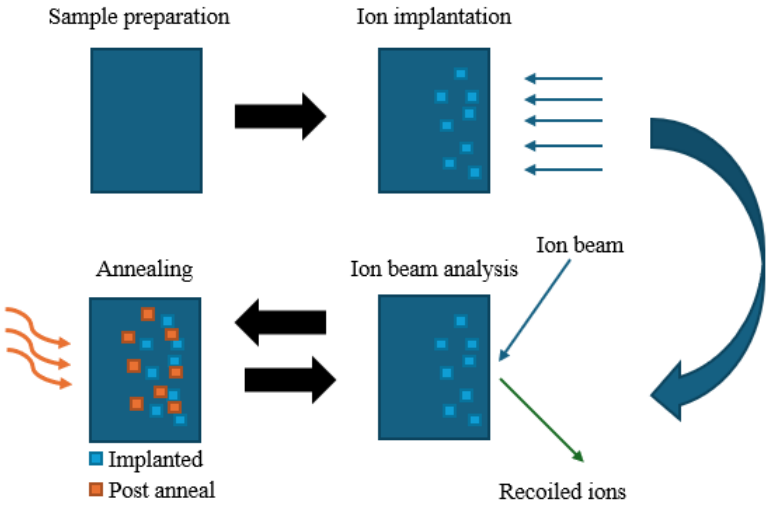

Figure 3.1: An illustration of the general process used to analyse the samples.

The samples were first prepared by grinding and polishing the surface at the Nuclear Fuels Laboratory at KTH and then analyzed using SEM, EDS, and XRD available at the Hultgern Laboratory at KTH. Thereafter the samples were implanted with the volatile element of interest using the 350kV ion implanter available at Uppsala University. ToF-ERDA measurements was then conducted at the Tandem laboratory at Uppsala University to assess the effects of the implantation. Subsequently, the samples were annealed and again analyzed with ToF-ERDA to assess the effects of the annealing. The annealing times were predicted by simulating the diffusion of the implanted species to get a first order estimate of the annealing times, as described in Section 3.5. The main focus of this thesis was on two types of samples with four types of

implanted ions. These were four sticks of ZrO_2, implanted with Xe, Kr, and iron (Fe), and five discs of UN implanted with Zr and Kr.

The choice of samples and ions was made from individual assessments of the samples that were at hand as well as what was needed from each sample. Table 3.1 shows which ions were implanted in each sample as well as the energies, doses, annealing times, and annealing temperatures.

Table 3.1: Summary of the ions, energies, doses, temperatures, and times used for the analysis of the samples in this thesis. It can be observed that some of the samples were not annealed, but only implanted due to the time-limited nature of the project which will be explained more in section 3.2.

Sample	Ion	Energy [keV]	Dose [cm^{-2}]	Temp [°C]	Anneal time [h]
ZrO_2-1	Xe + Kr	300	10^{17}	1200	9
ZrO_2-2	Xe	300	10^{17}	1200	9
ZrO_2-3	Kr	300	10^{17}	1200	9
ZrO_2-4	Fe	300	10^{17}	1600	14
UN_ref_MIT	Zr	330	$3.73 \cdot 10^{16}$	1100	48
UN_1_MIT	Zr	330	$9.7 \cdot 10^{15}$	-	-
UN_2_MIT	Kr	300	10^{17}	-	-
UN_05	Kr	300	10^{17}	-	-
UN_02	-	-	-	-	-

3.2 Samples

In this section, the process of preparing and analyzing each sample batch will be described. The ions implanted in each sample can be found in Table 3.1.

3.2.1 ZrO_2 samples

The initial batch of samples analyzed comprised four ZrO_2 sticks, provided by KTH. These samples were selected due to their similar properties to UO_2, making them a suitable surrogate for studying the diffusion of fission products within the fuel matrix. These samples were pre-characterised using XRD as detailed in section 3.4.4. From the XRD measurements, it could be shown that the ZrO_2 sticks had a density of 6.05 g/cm^3 due to the structure of the stick.

The ZrO_2 sticks were implanted with different ions using the 350 kV ion implanter at the Tandem Laboratory, as described in section 3.3. The implanted ions were one sample with Xe, one with Kr, one with both Xe and Kr and finally one with Fe. The implantation energy was set to 300 keV to achieve sufficient ion penetration depth. A dose of 10^{17} atoms/cm^2 was selected to ensure detectable levels of implanted ions for the subsequent ToF-ERDA measurements. During the implantations, the samples were cooled to around 100°C with water to reduce the effects of self-diffusion during implantation. The first three sticks were utilized to study the diffusion of volatile fission products in ZrO_2, while the Fe implanted stick, served as a test to examine metal

diffusion in a solid during annealing. The test aimed to determine if it was feasible to implant an excess of ions and anneal the sample to achieve a uniform distribution with approximately 1 part per thousand (ppt) over a full micrometer and was intended for use on the UN samples. The energies, doses, annealing temperatures, and times for each sample are summarized in Table 3.1.

The implantations were performed as described in section 3.3. For the first three samples implanted with Xe and Kr, half of each sample was covered with aluminium foil to prevent ion implantation on the covered regions, thereby retaining an unimplanted reference area. The Fe-implanted sample was not covered, allowing for ion implantation over the full sample. The implantation profiles are depicted in Figure 3.2.

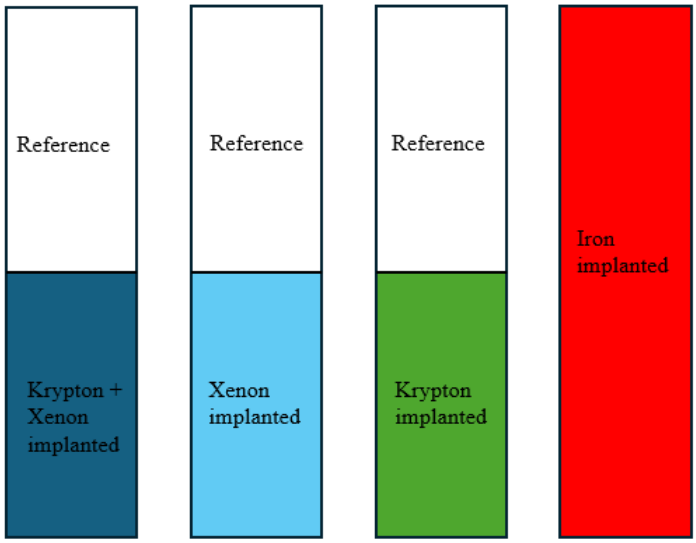

Figure 3.2: The implantation profiles for the implanted ZrO_2 sticks.

The samples were subsequently analyzed with ToF-ERDA and RBS as detailed in sections 3.4.1 and 3.4.2. For the ToF-ERDA measurements, a 40 MeV Gold beam was selected. Gold was chosen due to its heavy weight, and few isotopes, which provide a high current and sufficient scattering cross section. In the RBS analysis, a 4 MeV Helium beam was used. Light elements are usually preferred in RBS as described in section 2.7. After the initial analysis with ToF-ERDA and RBS, the samples underwent annealing in an oven at Uppsala University. During annealing, the samples were kept in an argon atmosphere. Post annealing, the samples were re-analyzed using ToF-ERDA with a 40 MeV gold beam to evaluate the effects of the annealing.

3.2.2 UN samples

The second set of samples analyzed consisted of five pellets of UN, provided by the Nuclear Fuels Lab at KTH. The pellets were sintered as explained by Charatsidou et al. and density measurements were performed. The measurement showed a density of 14.05 g/cm^3 for UN_ref_MIT, and 14 g/cm^3 for UN_1_MIT, UN_2_MIT, UN_02 and UN_05. The initial pellet, UN_ref_MIT was produced for a test run, and the four remaining samples were intended for scientific analysis

and subsequent characterization at MIT. The objective for this batch was to achieve implantation of one solid, and one gaseous fission product in the UN matrix, followed by annealing to attain an ion concentration of 1 ppt in the first micrometer of the sample. Due to the project's time constraints, only UN_ref_MIT was annealed [37].

The first step in the preparation of the samples was to cut, grind and polish the samples. All the samples were fabricated in the Nuclear Fuels Lab at KTH. Grinding was performed with Silicon Carbide papers under a constant water flow, with four different grit sizes: 280, 360, 600, and 1200 pp. Each grinding step lasted five minutes, with a 90-degree rotation between the steps to prevent striation. After grinding, the samples were subjected to a five-minute ultrasonic bath.

Polishing involved the use of cloths sprayed with a diamond polish of varying grit sizes: 9μm, 3 μm, 1 μm, and 0.5 μm, with each step lasting 10 minutes. Additionally, to make the samples prepared for EDS, an additional polishing step with colloidal scilica was performed for 10 minutes. In between each polishing step, the samples were put in an ultrasonic bath in water for 5 minutes. The final step included a ten-minute ultrasonic bath with ethanol followed by a twenty-minute ultrasonic bath in water. Subsequently, one sample was analyzed using XRD, SEM, and EDS, as explained in Section 3.4.3 and 3.4.4. Only one of the samples was analyzed since they originated from the same UN stick, and would therefore not show different results in the analysis with SEM and EDS.

Post SEM and EDS characterization, the samples were transported to Uppsala University for ion implantation using the 350kV implanter at the Tandem Laboratory, as described in 3.3. The first UN sample, named UN_Ref_MIT, was implanted with Zr. After the implantation, there was a clear gradient visible on UN_ref_MIT. The second batch included four samples: one sample was implanted with Zr, two were implanted with Kr, and one was retained as a reference to study room temperature oxidation. Of the Kr-implanted samples, one served as a reference for room temperature diffusion, and the other was designated for annealing.

The selection of ions was aimed at investigating the diffusion of both solid and gaseous fission products in the UN matrix. Zr and Kr were chosen due to their availability at the Tandem Laboratory and their relevance to the project. The chosen energies, doses, annealing temperatures, and times are summarised in Table 3.1. For sample UN_ref_MIT, the energy was maximized to achieve the highest possible dose, ensuring sufficient implanted concentration for subsequent ToF-ERDA and annealing. For samples UN_1_MIT and UN_2_MIT, the energies and doses were carefully selected through SRIM simulations to ensure enough implanted ions for achieving the desired 1 ppt in the first micrometer post-annealing. Additionally, UN_1_MIT and UN_2_MIT were covered with aluminium foil to preserve one side as a reference, resulting in the implantation profiles depicted in Figure 3.3.

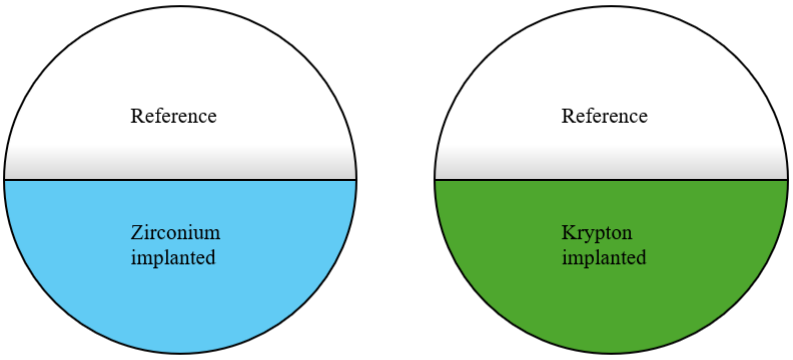

Figure 3.3: A schematic overview of samples UN_1_MIT and UN_2_MIT.

The same samples were subsequently analyzed using ToF-ERDA as described in Section 3.4.1 as wellindependent as SEM and EDS to quantify the implantations. By using both ToF-ERDA and SEM/EDS there were two independant measurements on the samples.

The first sample analyzed with SEM/EDS was sample UN_ref_MIT. This sample was analyzed with a line scan over the gradient that was implanted. Subsequently, samples UN_1_MIT and UN_2_MIT were analyzed over the line separating the implanted Kr and Zr. UN05 was not analyzed with SEM or EDS, since it was to be kept as a reference.

The ToF-ERDA was conducted with a 40 MeV Iodine (I) beam. I was selected for this analysis due to its single stable isotope and its ability to provide a high current with significant yield, which is particularly important when analyzing matrices containing U due to the high cross section. Sample UN_ref_MIT underwent annealing in an oven at KTH. However, during the removal of the sample, it disintegrated into a powder. Consequently, the sample could not be re-analyzed with ToF-ERDA.

3.3 Implantation

The implantations were performed using the 350kV ion implanter at the Tandem Laboratory. The implantations followed the same method through all implanted samples. Firstly, the samples were mounted onto the sample holders with copper tape to ground the samples and prevent charge buildup in the sample. Copper tape was used since it is conductive. After the samples were mounted, the ion source was started and the ions accelerated onto the target. To ensure that the dose would reach the expected values, the current had to be monitored during the whole process. A theoretical explanation of ion implantation can be found in Section 2.4.

3.4 Analysis Techniques

Before and after annealing, different analysis techniques were performed on each sample. These techniques have been described technically in Chapter 2, here follows a more practical description of the analysis techniques used in this project.

3.4.1 ToF-ERDA

In the Tandem laboratory beamline T4 there is a time of flight detector and an energy coincidence detector. This setup, along with the ion beam available from the Tandem Accelerator made ToF-ERDA possible. To perform ToF-ERDA, the samples had to be mounted on a specific holder that fits in the detection telescope for ToF-ERDA in the T4 beamline. To prevent dirt or damage buildup on the samples, gloves had to be used when mounting the samples. When the samples of interest had been mounted, a few reference points were added to be able to calibrate the detectors. The references used were silicon carbide (SiC), titanium nitride (TiN), copper (Cu), and molybdenum (Mo). After the acquisition was made the data was analyzed using Potku [31].

During the measurement, each sample was targeted with the ion beam until there were about 100,000 counts. The beam chosen for the analysis was dependent on what samples were to be analyzed. The beam was chosen in such a way that the elements of interest could be well distinguished in the produced time-energy coincidence plots. In this project either an I or Au beam was used. These ions provide good current as well as high scattering cross sections, since the cross section scales with the atomic number of the ion beam as seen in Equation (2.6). It is also important to choose an element which does not have many isotopes since this reduces the current. With these criteria in mind, Au and I were chosen to analyze the samples. The detector telescope is shown in Figure 3.4.

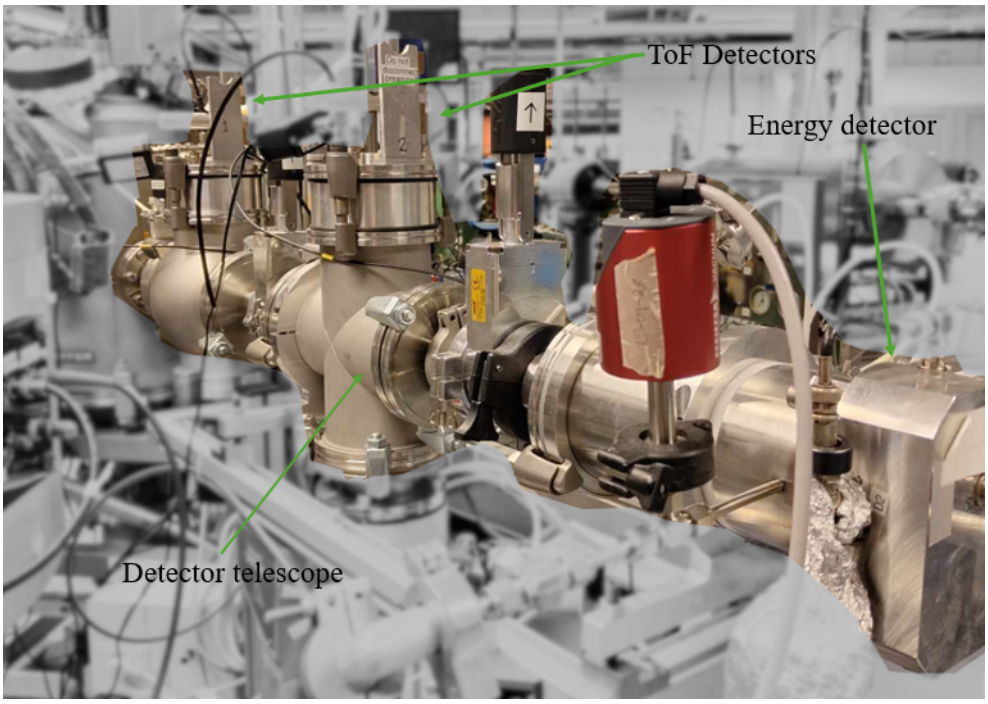

Figure 3.4: The end of the T4 Beamline available at Uppsala University, with the time of flight and energy detectors marked out.

3.4.2 RBS

To perform RBS, beamline T4 at the Tandem Laboratory at Uppsala University was used. The methodology for RBS is very similar to ToF-ERDA since it is in the same beamline. The samples were first mounted onto a sample holder and then placed into the vacuum chamber equipped

with a detector that detects ions backscattered at an angle of 165°. To prevent dirt buildup and damage to the samples, gloves were used when mounting the samples. A reference sample was also mounted to calibrate the detector. The reference chosen was a sample made with Au, Nickel (Ni), and Silicon (Si). The beam was chosen to be Helium at 4 MeV for the RBS analysis since it is light, gives good energy resolution, and is non-reactive. When the beam had been calibrated and aligned on the samples the data acquisition could start. When the data was finalized for all samples, it was analyzed using SIMNRA [38]. The detection chamber is shown in Figure 3.5.

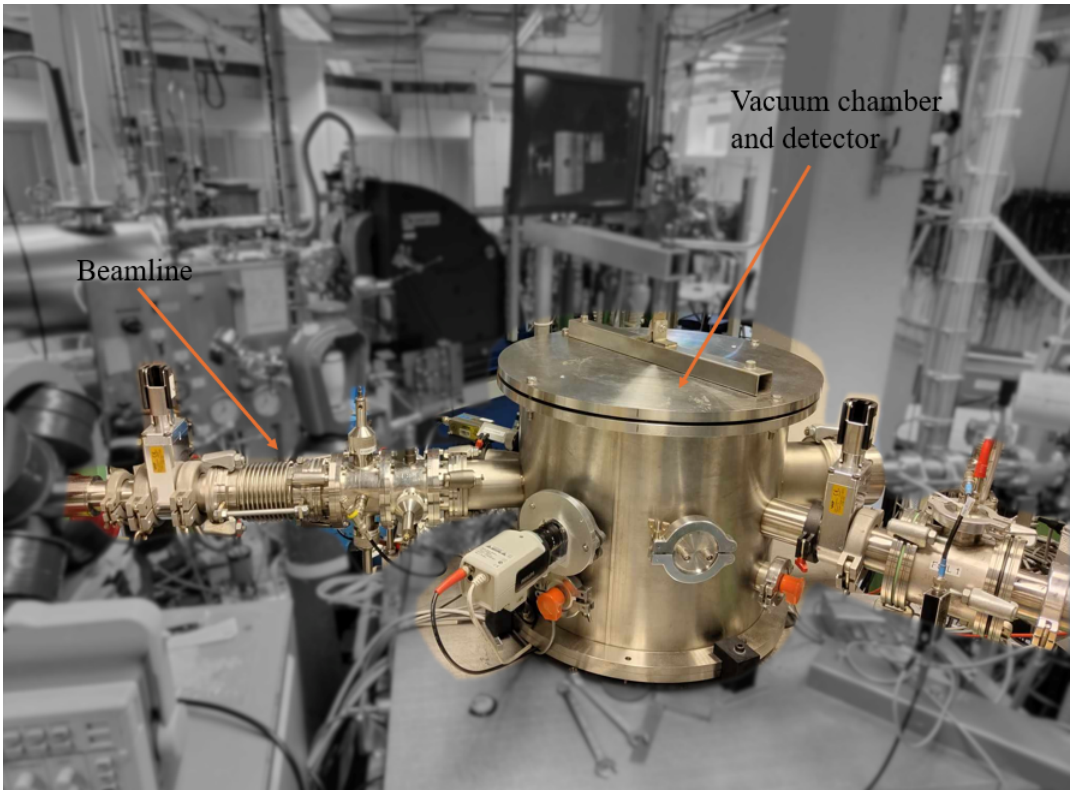

Figure 3.5: The T4 Beamline's RBS detector available at Uppsala University with the vacuum chamber marked.

3.4.3 SEM and EDS

SEM was performed at the Hultgren Laboratory at KTH. The analysis was performed by first mounting the samples onto a sample holder with carbon tape since carbon is conductive. When the samples had been mounted, the SEM chamber could be vented and the samples were put into the chamber. Subsequently, the electron source was started and the electrons were accelerated to 10 keV to provide an image of the sample. The samples were thoroughly analyzed and EDS was used to get compositional information as described in 2.8.

3.4.4 XRD

XRD was performed at the Nuclear Fuels lab at KTH. To perform XRD, the samples were first mounted onto the XRD sample holder. Subsequently, the samples were put into the XRD

chamber and it was made sure that the samples lay flat in relation to the incoming X-rays. When the experiment had been set up, the XRD scan was started and information was extracted.

3.5 Simulation

To provide an understanding of the range, straggle, amount implanted, and induced damage caused by the implantation, SRIM was used. In SRIM a TRIM (Transport of Ions In Matter) calculation was made for the different ions with the different energies. The simulations provided insight into what energies were to be used in the implantations. In total, five simulations were made. These were Xe, Kr, and Fe at 300keV into ZrO_2 as well as Zr at 330keV and Kr at 300keV into UN. The type of TRIM calculation was chosen to be "Ion Distribution and Quick Calculation of Damage" since it provided the information that was needed. After the parameters were chosen, the simulation was run until 100,000 ions had been simulated to get enough statistical significance [9].

To get a first estimate of the annealing times and temperature, Equation (2.13) with the diffusion coefficient modeled according to Equation (2.14), was solved using numerical methods. Since the idea was to be able to use SRIM data for input, equation (2.13) was solved numerically. The data from SRIM is not an analytic function, and therefore solving analytically would be impossible without approximations. In short, SRIM data is used as the input and lets the user select what temperatures and times for the annealing to simulate. The input data should be the output file RANGE from a SRIM TRIM calculation. Then, (2.13) is solved with the condition as described above with forward Euler in the time domain, and Central Difference in the space domain. These numerical methods were chosen since they are easily implemented, stable, and solve the problem fast. The boundary conditions chosen were Neumann boundaries on both sides so that diffusing atoms could freely escape from the surface.

The main factor that affected the output of the simulation was the diffusion coefficient taken from literature. The diffusion coefficient is varying with temperature since it follows Equation (2.14). A summary of the diffusion coefficients used is given in table 3.2.

Table 3.2: The different diffusion coefficients used in the project for each ion simulated.

Diffusing Ion	Target	E_a [eV]	D_0 [cm^2 s^{-1}]	Source
Xe	ZrO_2	3.26	$1.83 \cdot 10^{-6}$	[39]
Kr	ZrO_2	3.04	$8.11 \cdot 10^{-7}$	[39]
Fe	ZrO_2	2.3	$2.25 \cdot 10^{-6}$	[21]
Zr	UN	2.7	$6.9 \cdot 10^{-7}$	[40]

The diffusion coefficients for the Kr and Xe in ZrO_2 were taken from a study made in UO_2 since these were the only coefficients found in literature. Equivalently, the diffusion coefficient for Zr in UN was taken from a study made in thorium dioxide. Since the lattice structure is equal for the elements and the elements have similar properties, these diffusion coefficients could be used for simulation. It was further reinforced by the fact that the simulation was only to give a first estimate on the annealing times and thus not give exact results.

Chapter 4

Results

In this chapter, the most important results from analyzing each sample are presented. The data is structured such that each unique analysis or simulation result is presented in its own subsection.

4.1 ZrO_2 Samples

The ZrO_2 samples were implanted with different ions as shown in Table 3.1. To evaluate the effect of the implantations ToF-ERDA, RBS, and XRD were performed on the samples.

4.1.1 SRIM simulations

Analyzing the ZrO_2 sticks through the use of SRIM as explained in 3.5 was key to getting a first estimate of the average range and damage created by the implanted ions in the ZrO_2 Matrix. The results from the simulation are presented in Figure 4.1.

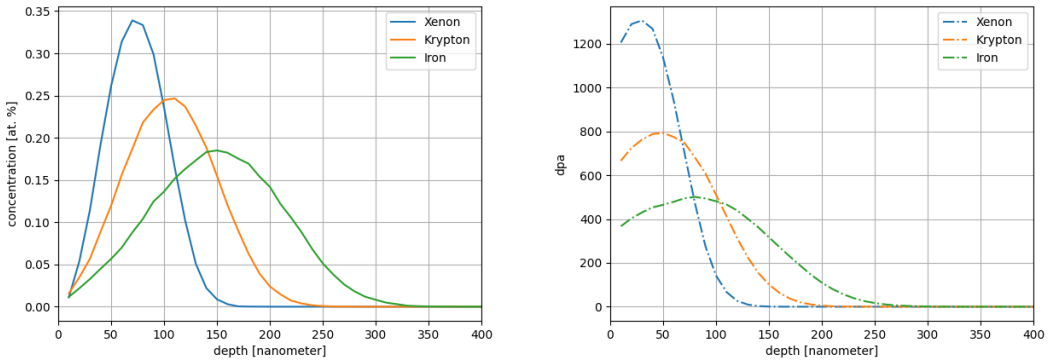

(a) Implanted concentrations

(b) Implanted damage

Figure 4.1: The results from the SRIM simulations of Xe, Kr and Fe at 300keV in ZrO_2.

As illustrated in Figure 4.1, the predicted average range for Xe, Kr, and Fe ions into ZrO_2 are 70 nm, 100 nm, and 140 nm, respectively. Regarding implantation-induced damage, the maximum dpa values are 1300 dpa for Xe, 800 dpa for Kr, and 500 dpa for Fe. Consequently, Xe ions are expected to cause the most significant lattice damage in the sample matrix.

4.1.2 XRD measurements

XRD measurements were performed on the unimplanted sides of Sample ZrO_2-1 as outlined in Section 3.2.1. The results from the measurement are presented in Figure 4.2.

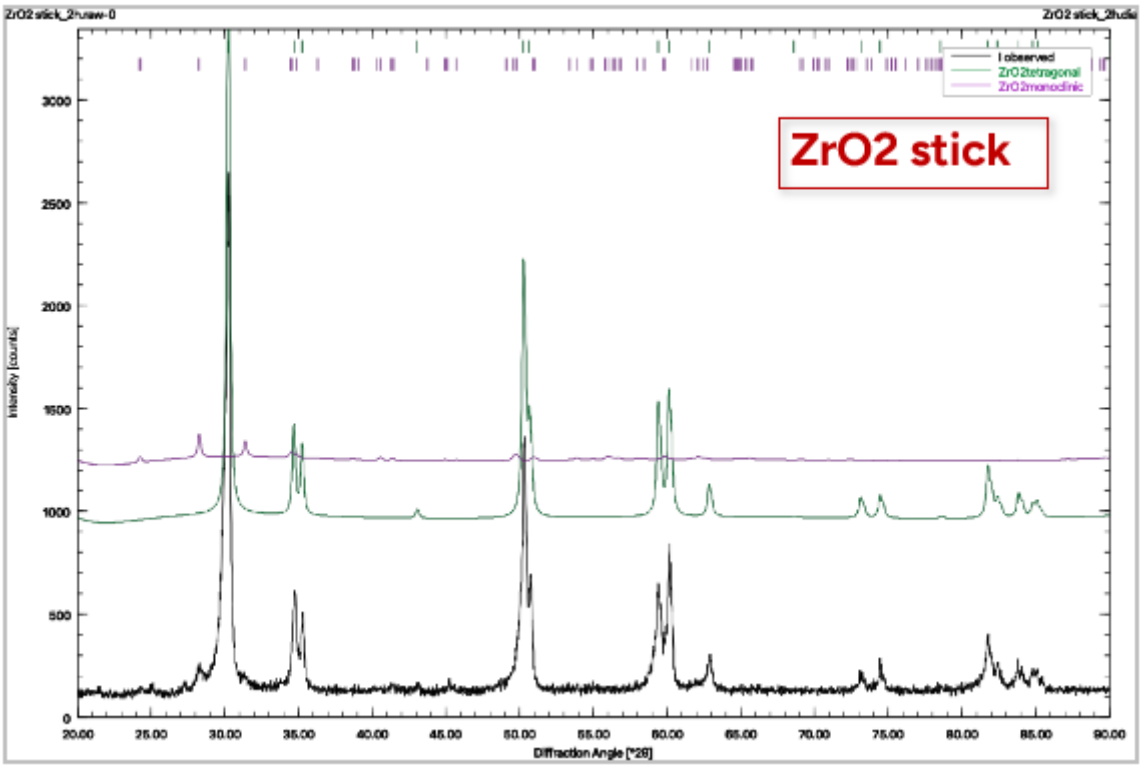

Figure 4.2: The results from the XRD measurement performed on the reference ZrO_2 stick.

Figure 4.2 shows that the sticks are made from two phases of ZrO_2, namely 7.8 wt. % monoclinic and 92.2 wt. % tetragonal. These are two common phases known for ZrO_2 that are stable.

4.1.3 ToF-ERDA measurements

The ZrO_2 samples were subject to ToF-ERDA, following the implantation. The chosen beam and energy can be found in Section 3.2.1. The time-energy coincidence plots produced by TOF-ERDA are given in Figure 4.3.

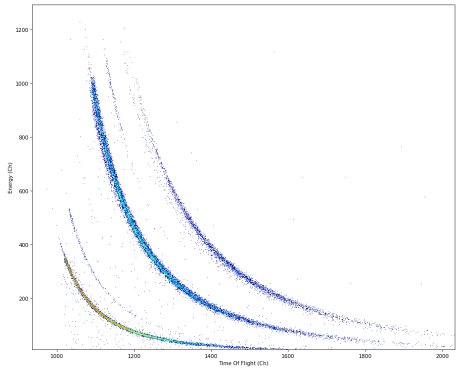

(a) Sample ZrO_2-1

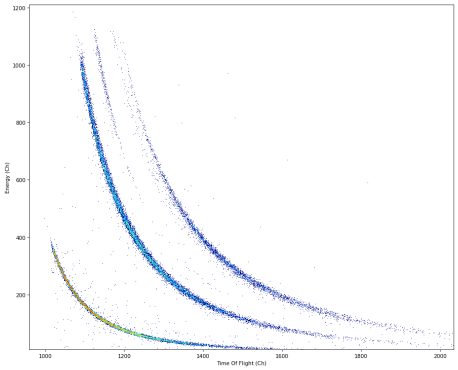

(b) Sample ZrO_2-2

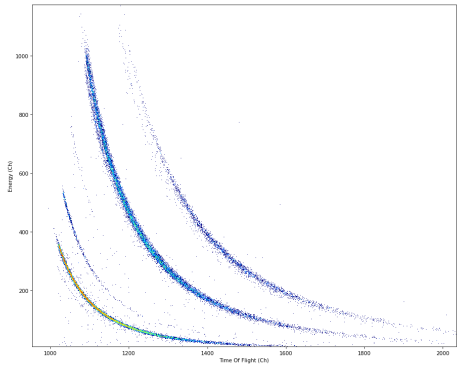

(c) Sample ZrO_2-3

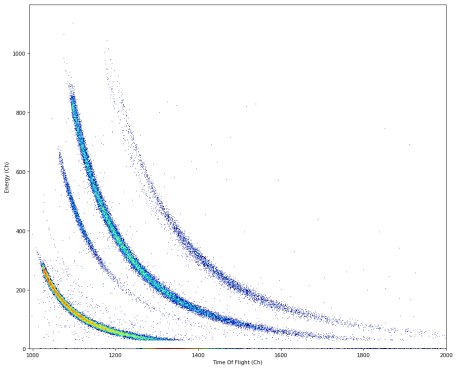

(d) Sample ZrO_2-4

Figure 4.3: The time-energy coincidence plots of the four ZrO_2 samples.

Figure 4.3a reveals that there are four elements present in all samples, as well as the implanted elements. The elements present in all samples were Zr, O, Hf and Au. The Au signal results from incident ion scattering on the sample, making the Au detectable. Hf is present since it is difficult to completely separate it from Zr.

Further examination of Figure 4.3b, indicates the presence of an element heavier than Zr, identified as the implanted Xe. It can also be seen that the Xe is accumulated near the surface and that the concentration is at its greatest in the middle of the distribution, just as predicted by Figure 4.1. Similarly, in Figure 4.3c, the implanted Kr can be seen near the Zr line.

In Figures 4.3c and 4.3a, an unexpected element between the O and Zr lines was detected. It was presumed that this was Alumiunium and it's origin will be further discussed in Section 5.1. In Figure 4.3d the implanted Fe was visible, along with the expected signals for Zr, O, Au, and Hf.

Finally, analyzing figure 4.3a, it can be observed that both the Kr and the Xe are present but Xe is appearing in lower concentrations. The lower concentrations were attributed to the diffusion of Xe out of the sample during implantation. From these time-energy coincidence plots, depth profiles were generated using the software Potku as illustrated in Figure 4.4.

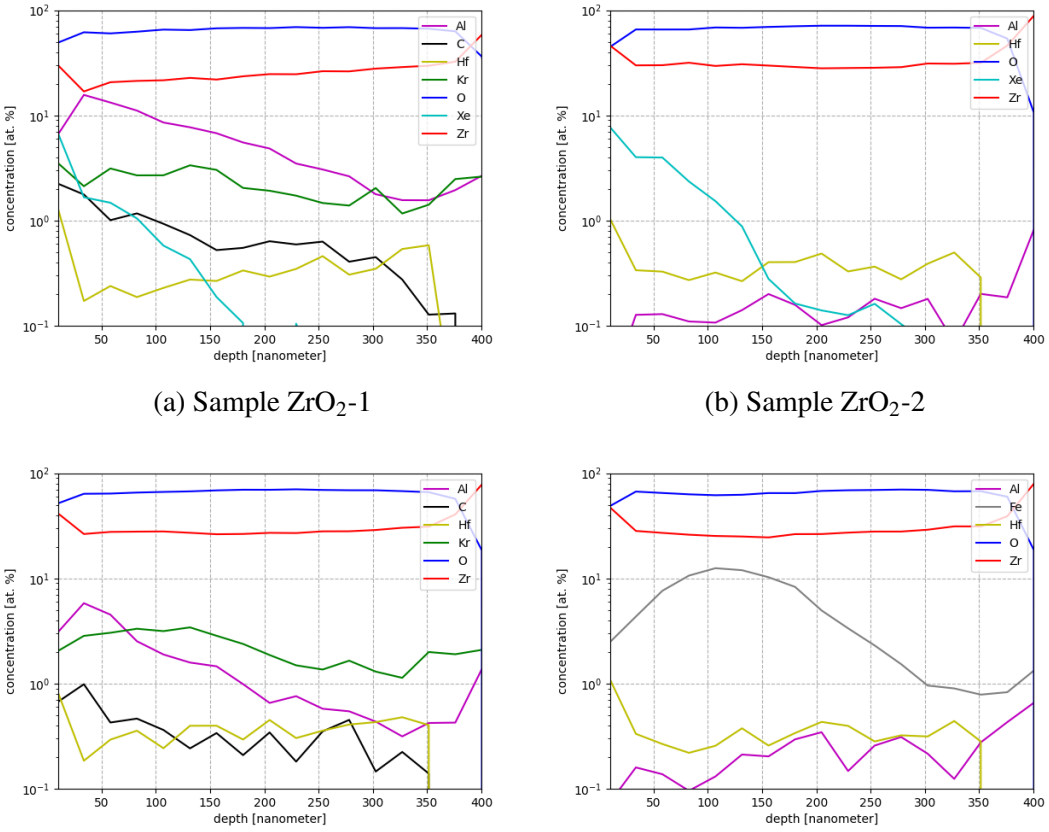

(a) Sample ZrO_2-1

(b) Sample ZrO_2-2

(c) Sample ZrO_2-3

(d) Sample ZrO_2-4

Figure 4.4: Depth profiles of samples ZrO_2-1 through ZrO_2-4 produced in Potku.

In Figures 4.4b through 4.4a, the x-axis was converted from atoms/cm^2 to nm using the reference density measured before implantation. Although the actual density may differ, the conversion enabled meaningful comparison with the SRIM simulations illustrated in Figure 4.1.

A significant observation is the presence of Al in two of the samples, depicted in Figure 4.4a, and in Figure 4.4c. The Al concentration reaches 14 at. % near the surface of the Xe/Kr implanted sample, and 7 at. % in the Kr implanted sample.

Further observation of Figure 4.4 confirms that the implantations went as expected. The average implantation ranges were 60 nm for Xe, 100 nm for Kr, and 120 nm for Fe. The measured implantation ranges are in agreement with what was predicted by the SRIM simulations in Figure 4.1. It was also observed that the Kr implantation in Sample ZrO_2-1 resulted in a significant reduction in the Xe concentration. The concentration of Xe was, at peak, 4 at % before Kr implantation, and was 2 at. % post-implantation.

From Figures 4.4b through 4.4a, the average concentration of each element in the range 0 nm to 460 nm was calculated. This data is shown in Tables 4.2 through 4.4. The statistical uncertainty analysis was made with the software Potku.

Table 4.1: Sample ZrO_2-1

Element	Concentration [at. %]
Zr	23.23 ± 0.14
O	64 ± 0.3
Xe	0.71 ± 0.03
Kr	3.08± 0.07
Hf	0.312 ± 0.012
Al	7.75± 0.13

Table 4.2: Sample ZrO_2-2

Element	Concentration [at. %]
Zr	30.17 ± 0.15
O	66.6 ± 0.3
Xe	1.53 ± 0.04
Hf	0.37 ± 0.02
Al	0.134 ± 0.011

Table 4.3: Sample ZrO_2-3

Element	Concentration [at. %]
Zr	26.7 ± 0.013
O	65 ± 0.4
Kr	3.35 ± 0.08
Hf	0.33 ± 0.02
Al	3.85 ± 0.11

Table 4.4: Sample ZrO_2-4

Element	Concentration [at. %]
Zr	27.34 ± 0.13
O	64.4 ± 0.3
Fe	6.82 ± 0.09
Hf	0.34 ± 0.02
Al	0.198 ± 0.011

4.1.4 RBS Analysis

To confirm the results that were found in the ToF-ERDA analysis, an RBS measurement was performed. The measurements provided another source to confirm the composition of the elements in some of the samples. As explained in Section 3.2.1, RBS was not performed on sample ZrO_2-4. The results of the fitted SIMNRA spectrum for sample ZrO_2-1 is shown in Figure 4.5. The fitted SIMNRA spectras for sample ZrO_2-2 and ZrO_2-3 can be found in Appendix B.

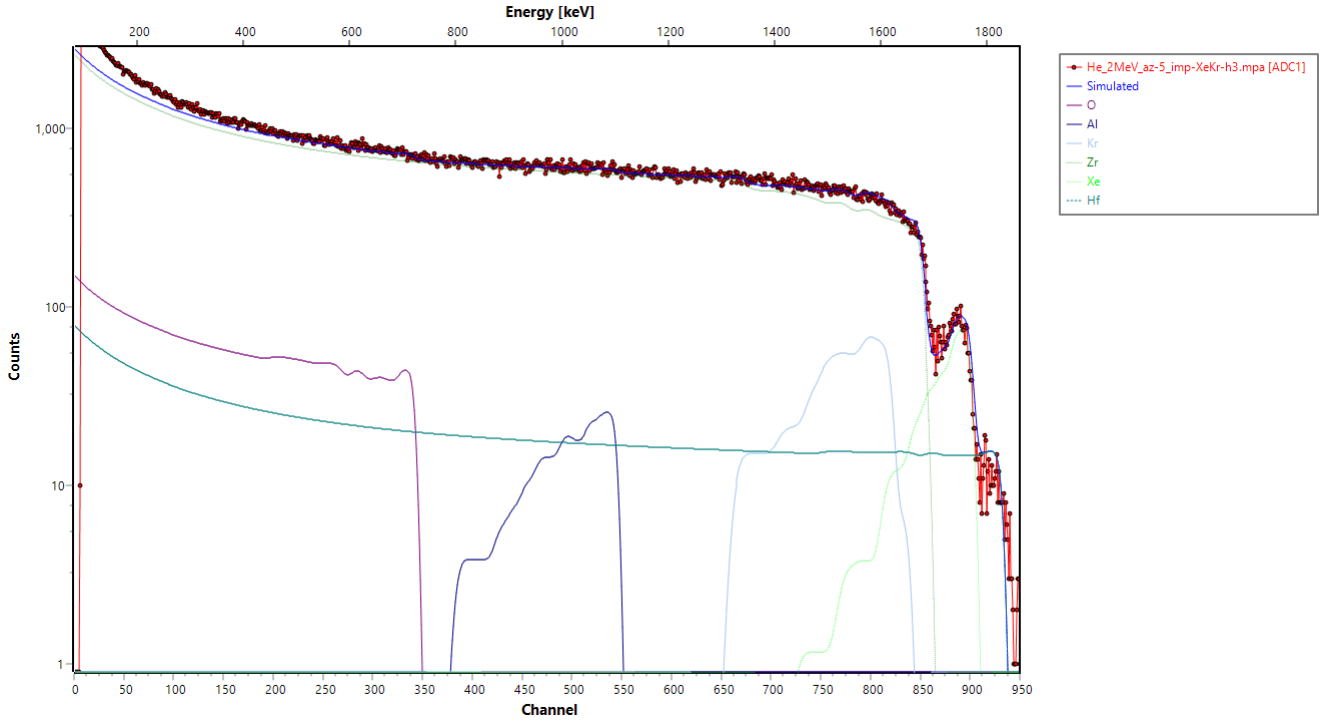

Figure 4.5: Fitted SIMNRA spectrum for sample ZrO_2-1.

The layers were created in such a way that the gradients corresponded to the measured distribution shown in Figure 4.4. The layer gradient in SIMNRA corresponds to the one measured with ToF-ERDA and further validates the measurements made by ToF-ERDA. To quantify the measurement, MULTISIMNRA was used to produce depth profiles. This is depicted in Figure 4.6

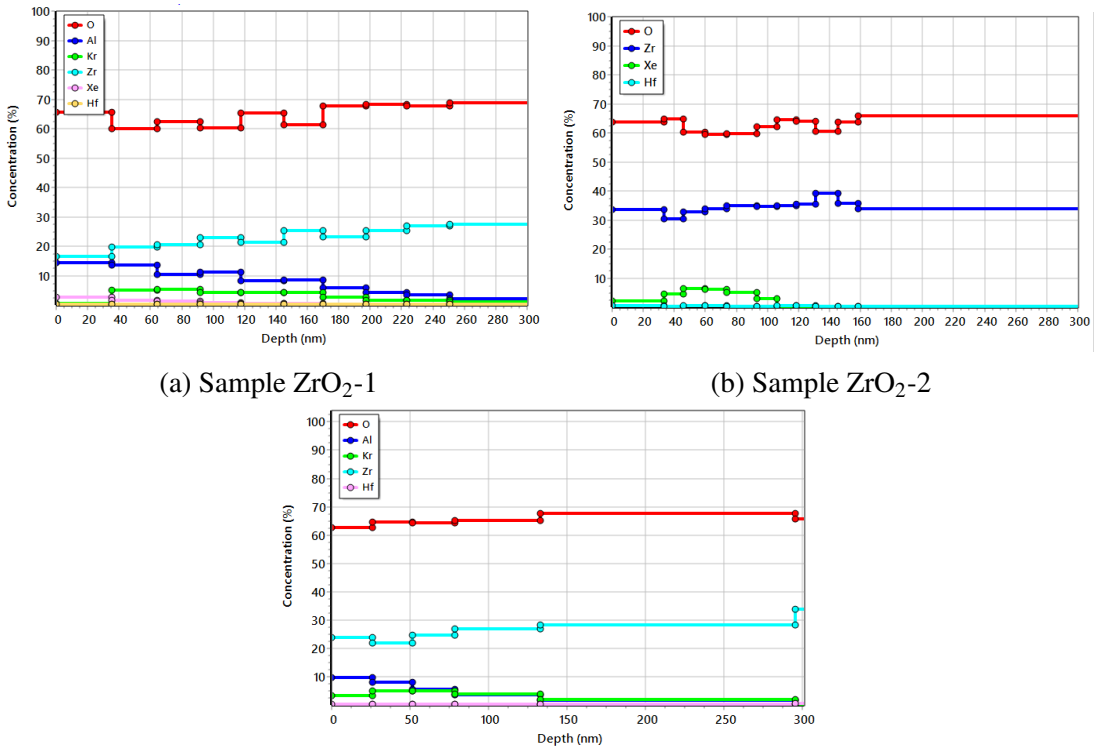

(a) Sample ZrO_2-1

(b) Sample ZrO_2-2

(c) Sample ZrO_2-3

Figure 4.6: Depth profiles produced from MULTISIMNRA for ZrO_2 samples ZrO_2-1, ZrO_2-2 and ZrO_2-3. The x-axis was rescaled to nanometers using the reference density to be able to compare to SRIM measurements.

According to the depth profiles shown in Figure 4.6, the average implantation ranges were 60 nm for Xe and 80 nm for Kr. The concentrations reached a maximum value of approximately 6 at. % for Xe and Kr. Comparing the values from the RBS measurement to the results from the SRIM simulation and the ToF-ERDA measurement shows agreement. This further validates the accuracy of the ToF-ERDA measurements.

4.1.5 Annealing Simulations

The critical question of how long the samples were to be annealed was calculated through the Python script described in Section 3.5. The simulations were performed at various times at 1200°C for the Xe and Kr implanted samples and at 1600°C for the Fe implanted sample. The results from the simulation are presented in Figure 4.7.

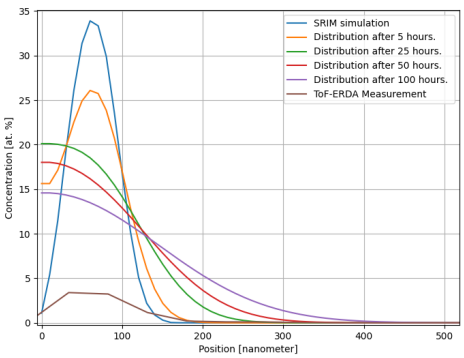

(a) Diffusion of Xe in ZrO_2 at 1200°C

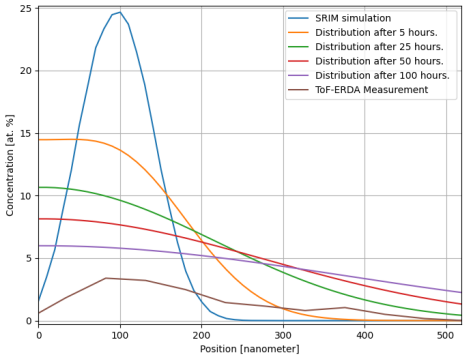

(b) Diffusion of Kr in ZrO_2 at 1200°C

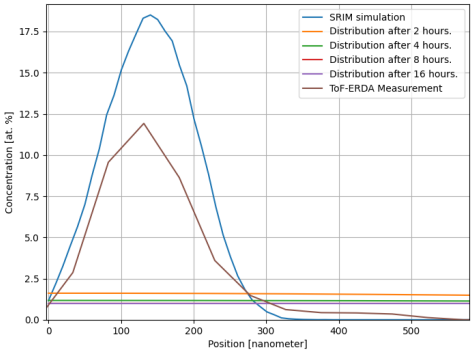

(c) Diffusion of Fe in ZrO_2 at 1600°C

Figure 4.7: Simulation results from solving Equation (2.13) with numerical methods for samples ZrO_2-2 to ZrO_2-4, compared with the measured data from ToF-ERDA.

In Figures 4.7a through 4.7c, the plot labeled ”Initial Distribution” represents the theoretical implantation distribution derived from SRIM data, as explained in Section 3.5. The SRIM distribution served as the basis for diffusion calculations performed by the Python code. The plot labeled ”ToF-ERDA measurement” shows the distribution measured using ToF-ERDA. As seen in Figure 4.7, the position of the implanted peaks aligns with the simulation, but the quantity differs. The average range and straggle match the expected values.

In Figure 4.7b, there is approximately 20 at. % difference in the maximum implanted amount, while Figure 4.7a shows a difference of 30 at. %. Finally, Figure 4.7c indicates a difference of 8 at %. It is evident in Figure 4.7c, that after 16 hours of annealing, the distribution should be completely flattend out. As mentioned in Section 3.2.1, this result was desirable for the test run, as to objective was to reach 1000 ppt over a full micrometer. It was decided that the Fe implanted sample was to be annealed at 1600 °C for 14 hours.

The other three samples, implanted with Xe, Kr, or both were annealed for shorter periods to understand the diffusion behavior of Xe and Kr in the material. Simulations were conducted for 5, 25, 50, and 100 hours. It was determined that 9 hours of annealing would be most beneficial, as it would allow for some diffusion of Xe and Kr without causing all implanted ions to leave the sample matrix during annealing.

A comparative analysis was conducted between the SRIM simulation output and the ToF-ERDA

measurement. To calculate the theoretical implanted ion concentration (TC), the backscattered ions from the SRIM simulations were considered. For Xe and Kr, this accounted for 5% of the ions, while for Fe, the backscattered ions were negligible (<0.1 %). Therefore, the theoretical implanted ion concentration was $9.5 \cdot 10^{16}$ atoms/cm^2 for Kr and Xe, and $1 \cdot 10^{17}$ atoms/cm^2 for Fe, since the input ion concentration was $1 \cdot 10^{17}$ atoms/cm^2. The TC was compared to the calculated implanted concentration (CC) which was determined by multiplying the height by the length of each bin. Before calculating CC, the noise was subtracted from the measurements and is presented in Table 4.5. The uncertainties were calculated from counting statistics as described in Appendix A.

Table 4.5: The theoretical implanted concentrations compared to calculated implanted concentrations for ZrO_2.

Sample	Implanted Ion	TC [atoms/cm^2]	CC [atoms/cm^2]	Ratio (CC/TC)
ZrO_2-2	Xe	$9.5 \cdot 10^{16}$	$(1.12 \pm 0.04) \cdot 10^{16}$	0.12 ± 0.01
ZrO_2-3	Kr	$9.5 \cdot 10^{16}$	$(2.96 \pm 0.06) \cdot 10^{16}$	0.31 ± 0.01
ZrO_2-4	Fe	$1 \cdot 10^{17}$	$(6.77 \pm 0.1) \cdot 10^{16}$	0.71 ± 0.01

4.1.6 Post Annealing ToF-ERDA measurements

Annealing of the implanted ZrO_2 sticks was performed, as described in Chapter 3. Post-annealing, the samples were again subject to ToF-ERDA with an analyzing beam as described in 3.2.1. The time-energy coincidence plots produced from the measurement are shown in figure 4.8.

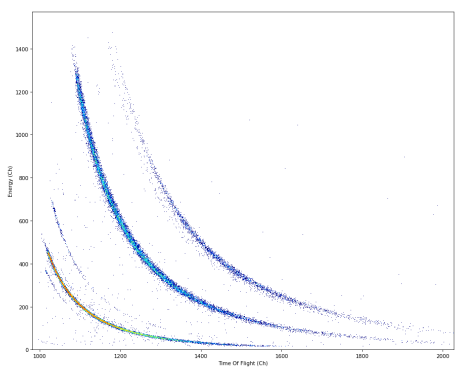

(a) Sample ZrO_2-1

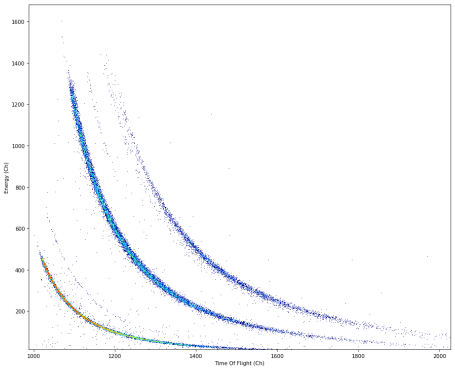

(b) Sample ZrO_2-2

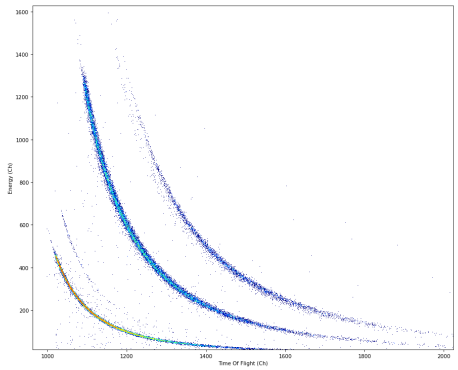

(c) Sample ZrO_2-3

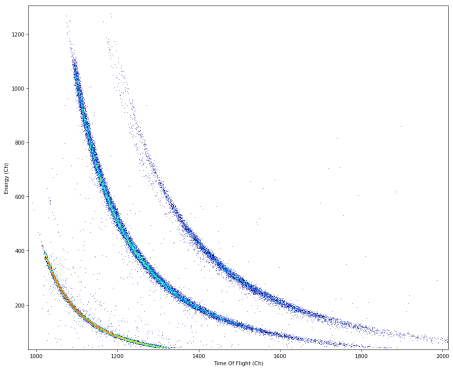

(d) Sample ZrO_2-4

Figure 4.8: The time-energy coincidence plots of the four different samples, after annealing.

In Figure 4.8, the expected lines for Zr, O, Au, and Hf are present. When comparing Figure 4.3 with Figure 4.8, several noticable differences emerge. Firstly, the concentration of Xe in Figure 4.8b, Kr in Figure 4.8c and Xe and Kr in Figure 4.8a have decreased. The concentration of Fe in Figure 4.8d is not present. Secondly, the concentration of Al observed in the pre-annealing measurements has significantly reduced. To quantify the reduction and re-distribution of the concentrations, depth profiles were created for each sample. These are shown in Figure 4.9.

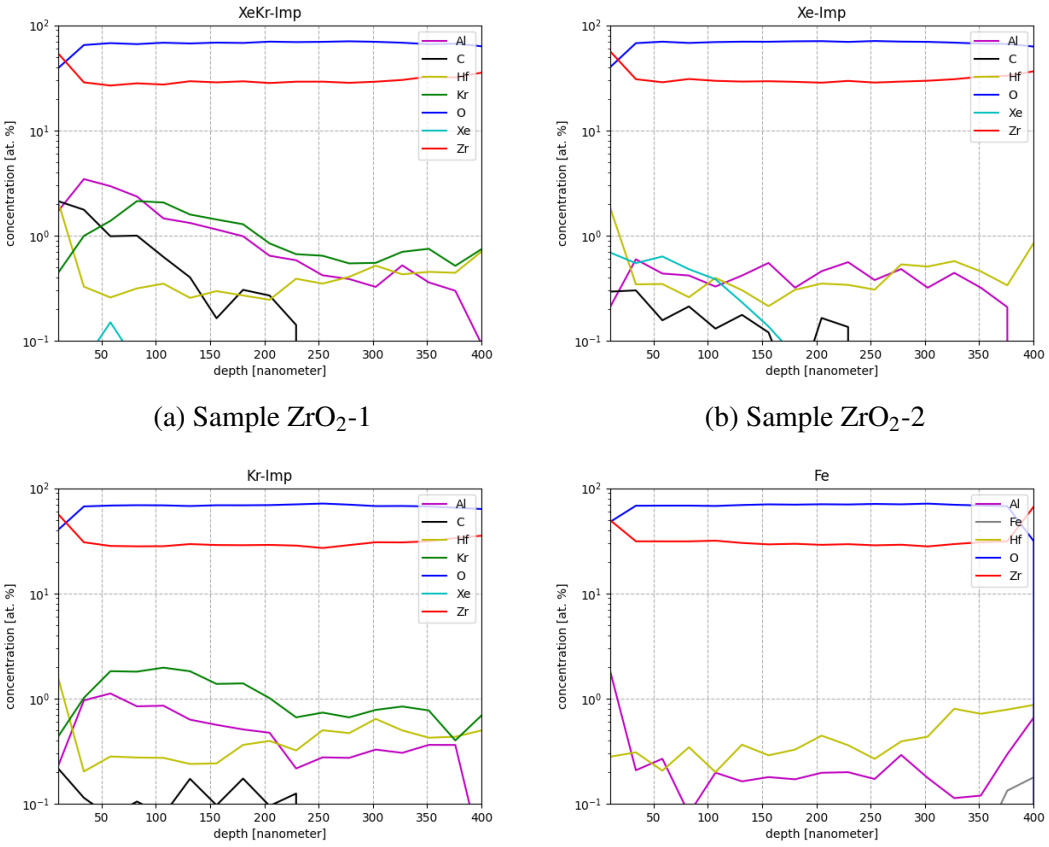

(a) Sample ZrO_2-1

(b) Sample ZrO_2-2

(c) Sample ZrO_2-3

(d) Sample ZrO_2-4

Figure 4.9: Depth profiles of samples ZrO_2-1 through ZrO_2-4 produced in Potku, after annealing.

In Figures 4.9b through 4.9a, the x-axis was converted from atoms/cm^2 to nm using the reference density measured before the implantation to be able to compare to the SRIM simulations. As shown in Figure 4.9, the predictions based on the time-energy coincidence plots appear to be accurate. The implanted concentrations have reduced and slightly flattened out during the annealing process. Notably, this also applies to the Al content in the matrix. The implanted Xe in Figure 4.9b has decreased from 4 at. % to 0.5 at. %, the implanted Kr in Figure 4.9c has reduced from 3.5 at. % to 2 at. % and the implanted Fe dropped from 12 at. % to 0 at. %.

To further analyze the impact of the annealing on the ions of interest in each sample, depth profiles were created to compare the pre-annealing concentration and post-annealing concentrations. The results are presented in Figure 4.10.

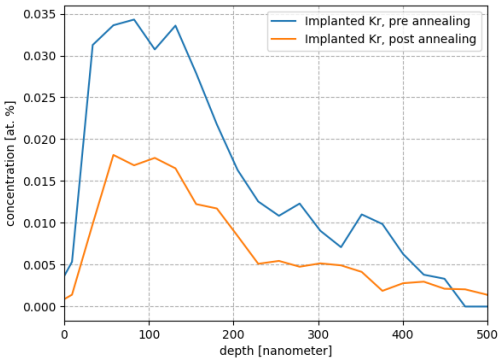

(a) Kr in ZrO_2-2, before/after annealing

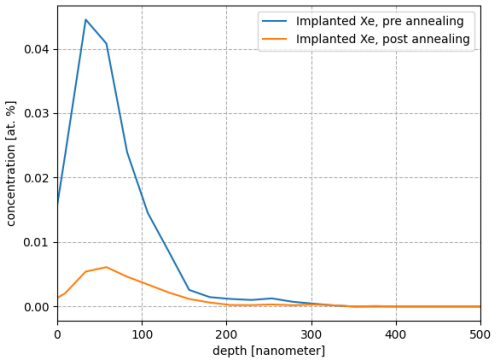

(b) Xe in ZrO_2-3, before/after annealing

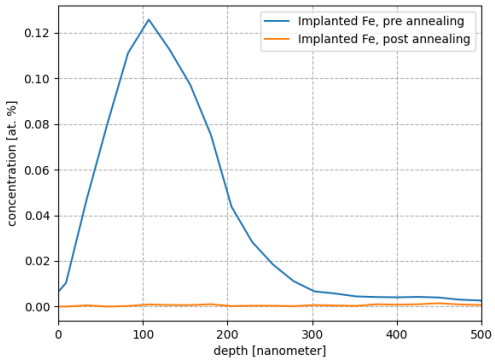

(c) Fe in ZrO_2-4, before/after annealing

Figure 4.10: Depth profiles of implanted ions in samples ZrO_2-2 through ZrO_2-4, before and after annealing at 1200°C or 1600°C for 9 or 14 hours.

In Figure 4.10, it is evident that most of the reduction in concentration results from the gas release of the implanted species, since the shape of the curves remains consistent while the concentration decreases. For the Fe implanted sample, all implanted Fe diffused out during annealing due to the excessive time and temperature caused by misinterpretation of the results from the simulation. To quantify the loss of implanted ions during annealing, the average implanted concentration in at. % from 0 nm to 500 nm was compared before and after annealing. The comparison is shown in Table 4.6.

Table 4.6: Kr, Xe, and Fe concentrations, as measured by ToF-ERDA pre- and post-annealing. Uncertainties are based on counting statistics as described in Appendix A.

Sample	Implanted Ion	Pre-anneal [at. %]	Post-anneal [at. %]	Difference
ZrO_2-1	Xe	0.49 ± 0.02	0.032 ± 0.006	-93%
ZrO_2-1	Kr	2.21 ± 0.05	1.1 ± 0.03	-50%
ZrO_2-2	Xe	1.24 ± 0.04	0.196 ± 0.014	-85%
ZrO_2-3	Kr	2.35 ± 0.05	1.16 ± 0.03	-50%
ZrO_2-4	Fe	5.9 ± 0.08	0.053 ± 0.008	-99.1%

4.2 UN Samples

The second set of samples analyzed comprised five pellets of UN, as detailed in Section 3.2.2. The first sample, UN_ref_MIT, was implanted with Zr. Post-implantation, a distinct implantation gradient was visible. The gradient was attributed to the fact that the beam had not hit the full sample and therefore only implanted half of it. The gradient is illustrated in Figure 4.11. To analyze the gradient, ToF-ERDA was performed at four different spots on the sample, marked in Figure 4.11.

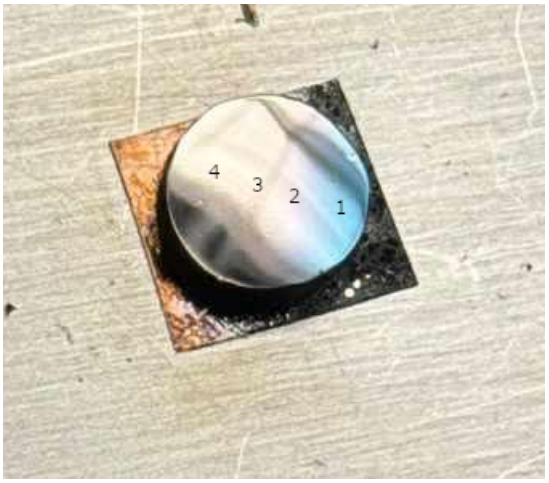

Figure 4.11: The implanted gradient in sample UN_ref_MIT and the four analyzed spots.

4.2.1 SRIM simulations

To achieve an understanding of the average range and implanted damage in the UN matrix for the different ions and energies presented in Table 3.1, SRIM simulations were conducted. The simulation results are shown in Figure 4.12 for sample UN_ref_MIT and in Figure 4.13 for the remaining samples.

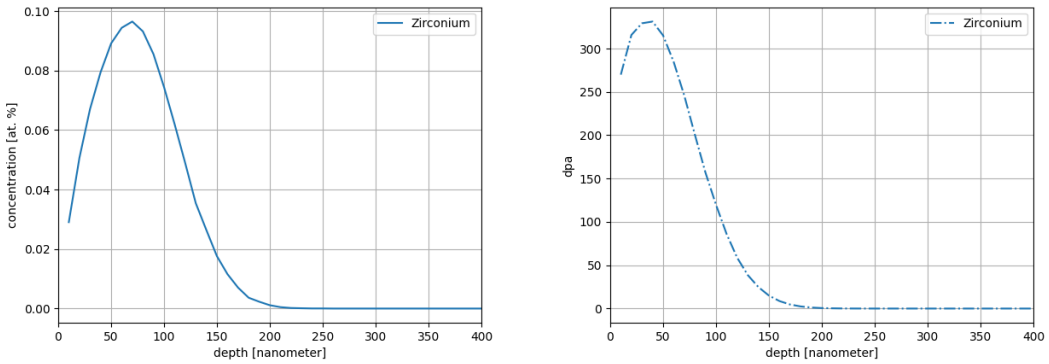

(a) Implanted concentration

(b) Implanted damage

Figure 4.12: SRIM simulation of Zr and Kr, with parameters as presented in Table 3.1 for UN_ref_MIT.

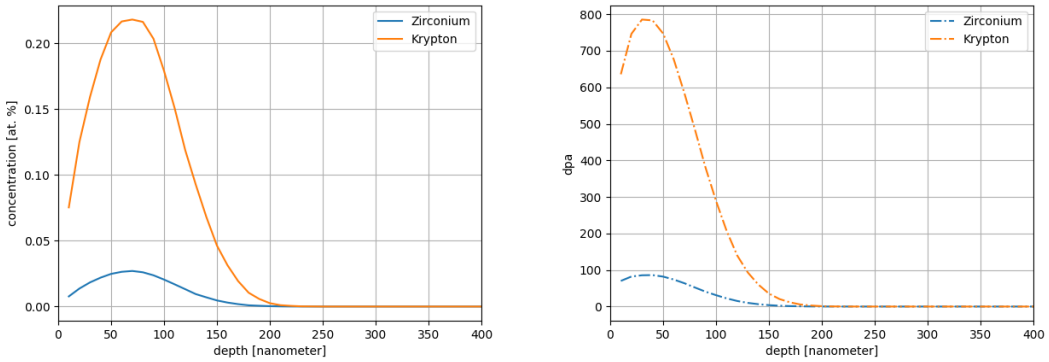

(a) Implanted concentration (b) Implanted damage

Figure 4.13: SRIM simulation of Zr and Kr, with parameters as presented in Table 3.1 for UN_1_MIT, UN_2_MIT and UN_05.

In Figure 4.12, the theoretical implantation profile for UN_ref_MIT indicates an average range of 80 nm with a concentration of 10 at. %. The maximum implantation-induced damage is estimated to be 330 dpa. Equivalently, in Figure 4.13, the predicted average range for UN_1_MIT was also 80 nm, with a concentration of 2.5 at. % and a dpa of 100, while for UN_2_MIT and UN_05, the predicted average range is 100 nm with concentrations of 23 at %. The corresponding maximum implantation-induced damage is approximately 800 dpa for both UN_2_MIT and UN_05.

4.2.2 Pre-characterization

The UN samples were characterised with XRD and SEM prior to implantations as explained in Section 3.2. Only one sample had to be pre-characterised as they originated from the same UN stick. The results from the XRD and SEM is shown in Figure 4.14.

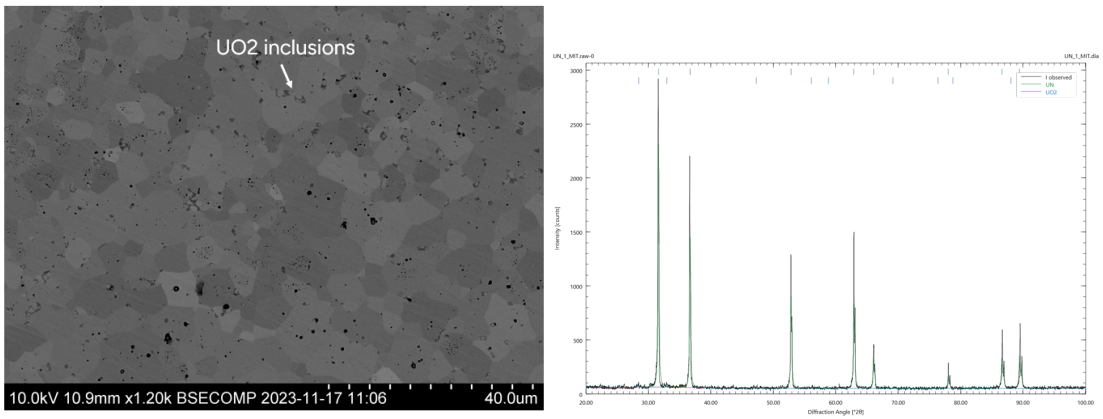

(a) SEM Image of the UN pellet (b) XRD scan of the UN

Figure 4.14: SEM image and XRD measurements of the reference UN sample.

The XRD scan and the SEM image show that the sample is 98.59 % UN and 1.41 % UO_2. The UO_2 inclusions in the sample matrix can be seen as indicated in Figure 4.14a. By further

investigation of Figure 4.14a it can be seen that the grains are about 5 μm in diameter.

4.2.3 ToF-ERDA measurements

As the UN samples had been implanted, they were subject to ToF-ERDA, as described in Section 3.2.2. The time-energy coincidence plots produced from the measurements of sample UN_ref_MIT is shown in Figure 4.15.

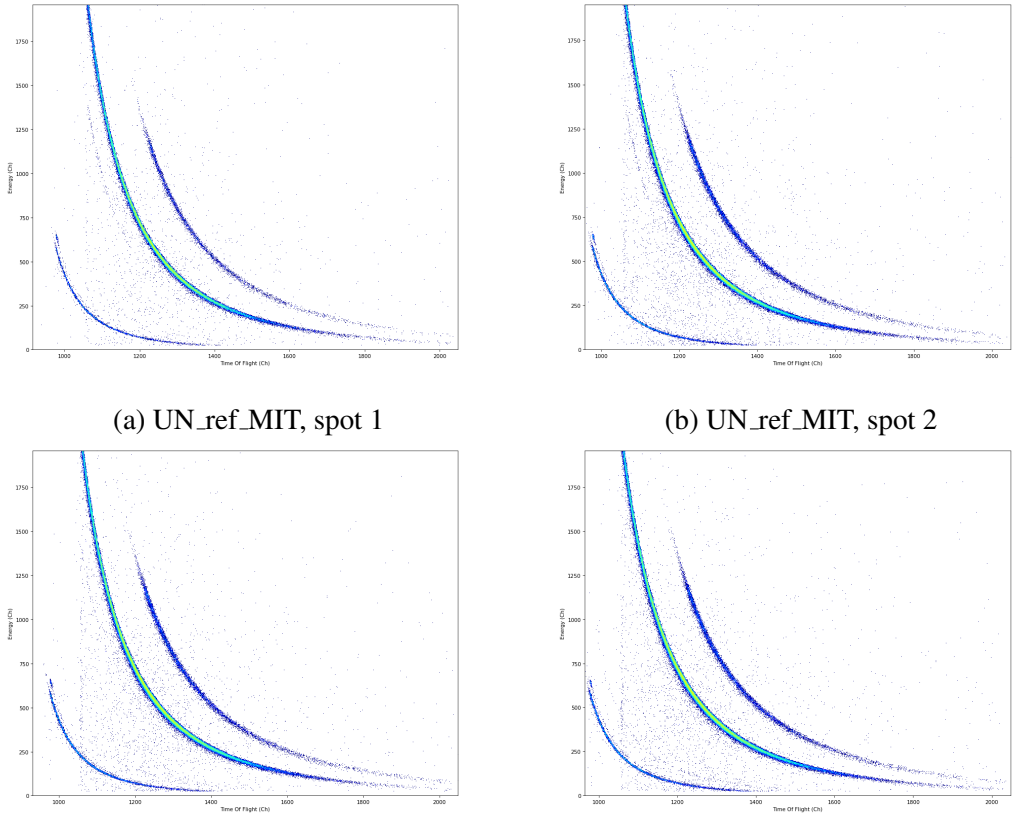

(a) UN_ref_MIT, spot 1

(b) UN_ref_MIT, spot 2

(c) UN_ref_MIT, spot 3

(d) UN_ref_MIT, spot 4

Figure 4.15: The time-energy coincidence plots of sample UN_ref_MIT, aimed at four different parts of the sample as depicted in Figure 4.11.

The time-energy coincidence plots depicted in Figure 4.15 reveal the presence of Nitrogen (N), O, Zr, I and U. The I signal stems from the scattered incident ion beam onto the detectors. Due to the gradient in the implanted Zr, the Zr line in Figures 4.15a through 4.15d are less and less visible. To quantify the measurements made, Potku was used to create elemental depth profiles. The depth profiles are presented in Figure 4.16.

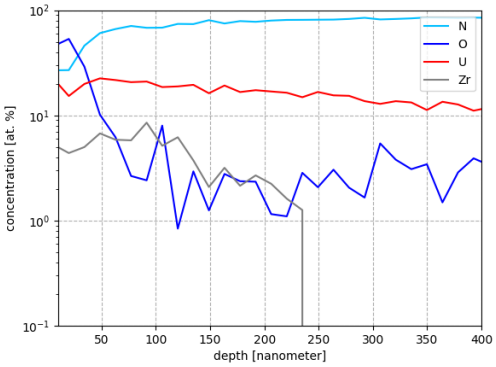

(a) Sample UN_ref_MIT, spot 1

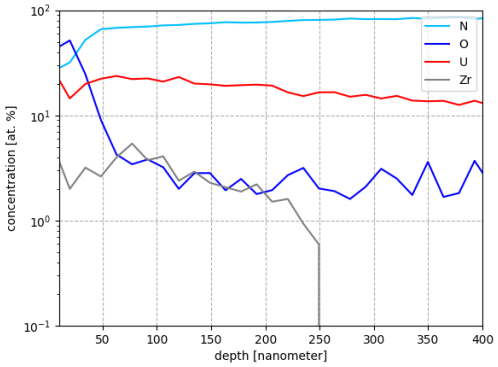

(b) Sample UN_ref_MIT, spot 2

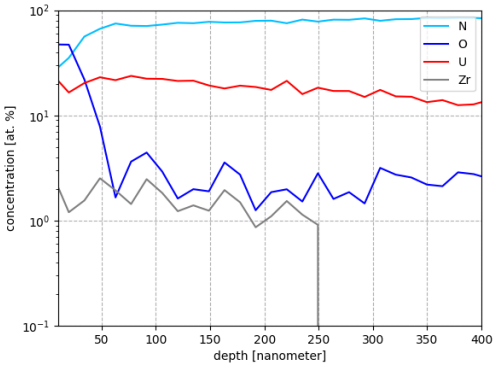

(c) Sample UN_ref_MIT, spot 3

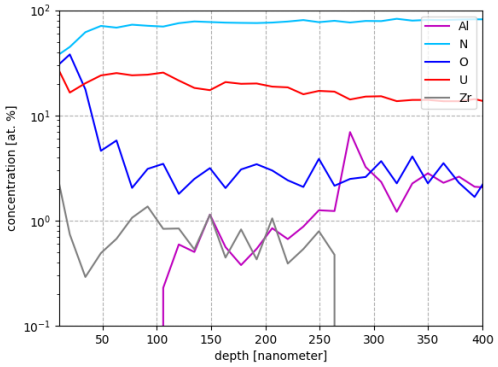

(d) Sample UN_ref_MIT, spot 4

Figure 4.16: Depth profiles of sample UN_ref_MIT produced in Potku, aimed at four different parts of the sample as depicted in Figure 4.11.

Figure 4.16, reveals a significant oxidation layer on the surface of the implanted samples. Additionally, as predicted from the time-energy coincidence plots, a gradient in the implanted concentration of Zr is observed. The concentration of Zr is approximately 2.5 at. % in spot 1, and reaches about 1 at. % in spot 4. Notably, the measurements indicate approximately 20 at. % U and 70 at. % N present in the matrix. The underlying reason for these findings will be evaluated in Chapter 5.

A comparative analysis was conducted between the SRIM simulation output and the actual ToF-ERDA measurement in spot 1 to assess the consistency with the predictions made from SRIM. The measured concentration was used to calculate the implantation density by multiplying the height with the width of each bin, which was then compared to the value used in the SRIM simulation. The results of the comparison are presented in Figure 4.17.

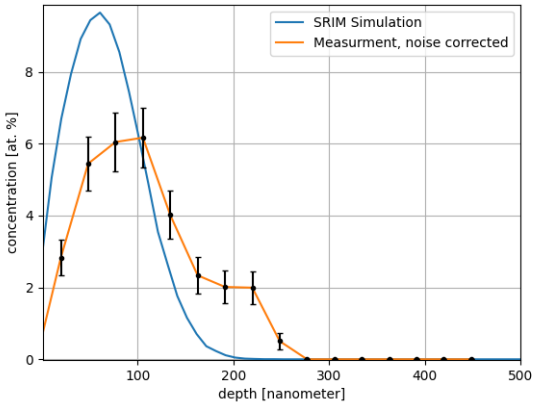

Figure 4.17: A comparison made between the SRIM simulation and ToF-ERDA measurement for sample UN_ref_MIT with error bars calculated through counting statistics.

The input concentration in the SRIM simulation was $3.73 \cdot 10^{16}$ atoms/cm^2. Noting that about 3.5% of the Zr ions backscatter, the adjusted implanted concentration was $3.59 \cdot 10^{16}$ atoms/cm^2. However, the calculations based on the measured spectrum indicated that the actual implanted concentration was $(2.93 \pm 0.19) \cdot 10^{16}$ atoms/cm^2. In Figure 4.17, the noise in the measurement was subtracted from the actual measurement, and the uncertainty propagation was made from counting statistics as described in Appendix A.

A summary of the average concentration from 0 nm to 400 nm is presented in tables 4.7 through 4.10. The statistical uncertainty analysis was made by counting statistics.

Table 4.7: Zr imp UN Spot 1

Element	Concentration [at. %]
U	17.9 ± 0.2
N	71.8 ± 0.7
O	7.7 ± 0.3
Zr	2.62 ± 0.14

Table 4.8: Zr imp UN Spot 2

Element	Concentration [at. %]
U	19.23 ± 0.12
N	72.2 ± 0.3
O	7.0 ± 0.2
Zr	1.58 ± 0.08

Table 4.9: Zr imp UN Spot 3

Element	Concentration [at. %]
U	19.61 ± 0.12
N	73.2 ± 0.5
O	6.2 ± 0.2
Zr	0.97 ± 0.06

Table 4.10: Zr imp UN Spot 4

Element	Concentration [at. %]
U	19.61 ± 0.12
N	73.1 ± 0.5
O	5.4 ± 0.2
Zr	0.48 ± 0.05
Al	1.37 ± 0.05

Tables 4.7 through 4.10 reveal that the oxidation appears to correlate with the implantation concentration, decreasing as the implanted Zr concentration reduces. The mechanism creating the oxide layer will be discussed in section 5.2.

The second set of samples, UN_02, UN_05, UN_1_MIT and UN_2_MIT were implanted and

analyzed as described in section 3.2.2. The time-energy coincidence plots produced from the measurements are presented in figure 4.18

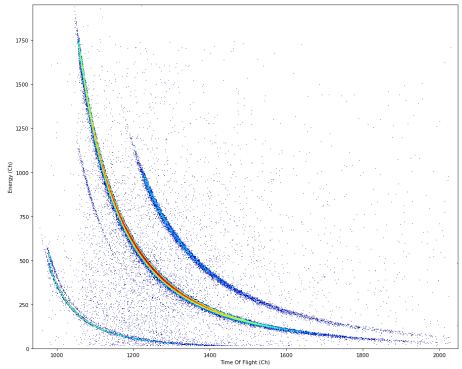

(a) Sample UN-05

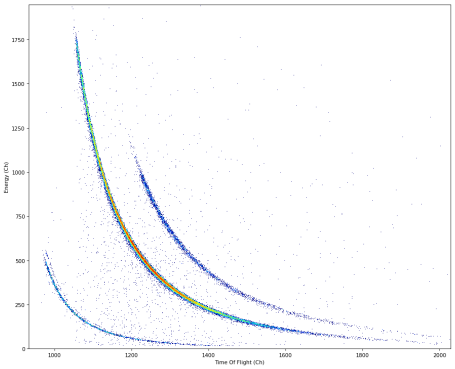

(b) Sample UN-02

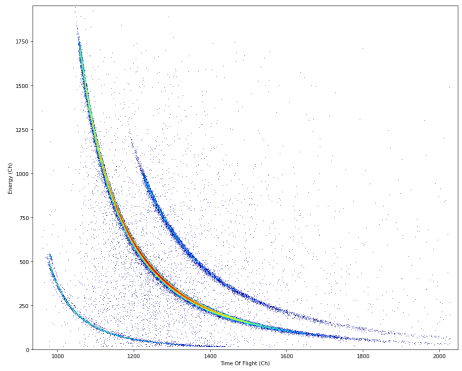

(c) Sample UN_1_MIT

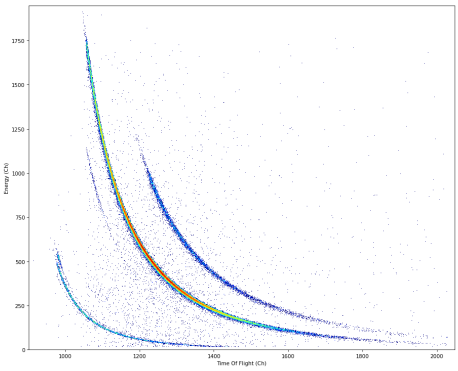

(d) Sample UN_2_MIT

Figure 4.18: The time-energy coincidence plots of samples UN_1_MIT, UN_2_MIT, UN-02 and UN-05

Figure 4.18 reveals the presence of N, O, I, and U, as these were present in the matrix prior to implantation. Additionally, the analysis shows that sample UN_05 and sample UN_2_MIT had an implanted Kr concentration, UN_1_MIT had an implanted Zr concentration, and UN_02 had no implanted concentrations, as expected. The time-energy coincidence plots also revealed that there was carbon contamination present in the samples. To quantify the implantations, Potku was used to generate depth profiles. The elemental depth profiles are shown in figure 4.19.

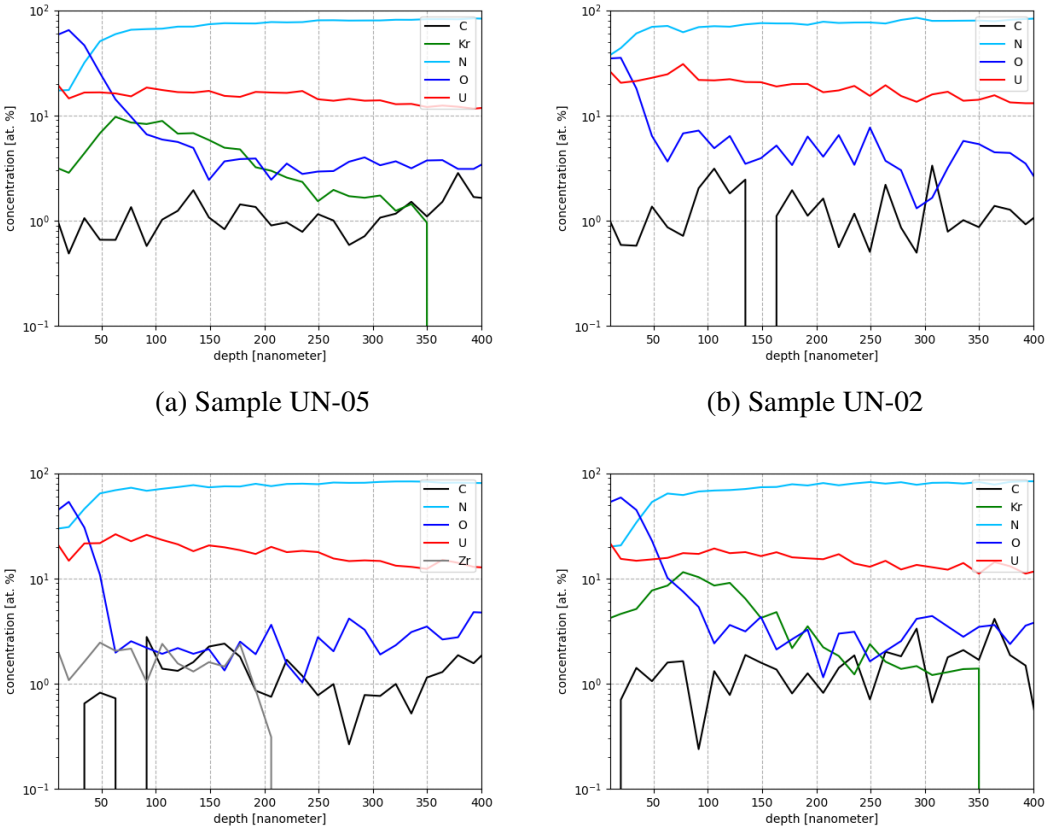

(a) Sample UN-05

(b) Sample UN-02

(c) Sample UN_1_MIT

(d) Sample UN_2_MIT

Figure 4.19: Depth profiles of samples UN-05, UN-02, UN_1_MIT, and UN_2_MIT produced in Potku.

The depth profiles depicted in Figure 4.19 indicate that the average range for the implanted Kr in samples UN_05 and UN_2_MIT was 90 nm, with an implanted concentration of 8 at. %. For the Zr implanted sample, UN_1_MIT, the average range was approximately 60 nm and was at a concentration of 2 at. %. While the range corresponded well with predictions by SRIM, the actual concentration of Kr was lower than predicted by SRIM. The lower concentration is to be expected due to the volatile nature of gaseous fission products as explained in section 2.3.1.

As done in the previous measurement, a comparative analysis between the SRIM simulation output and the actual ToF-ERDA measurement was conducted for the implanted samples. The measured concentration was used to calculate the implantation density which was compared to the value used in the SRIM simulation. The results from the comparison are presented in Figure 4.20. Before plotting, the noise in the measurement was subtracted from the measurement, and the uncertainty was calculated through counting statistics as described in Appendix A.

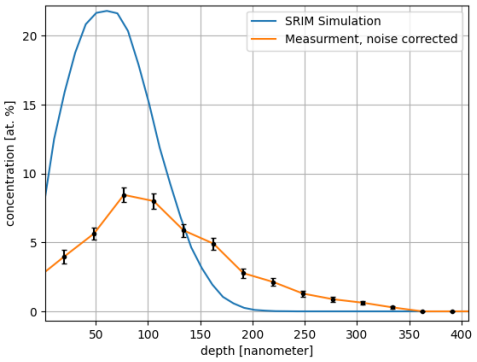

(a) UN-05, implanted with Kr

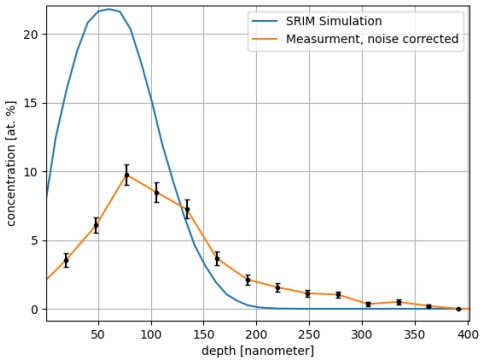

(b) UN_2_MIT, implanted with Kr

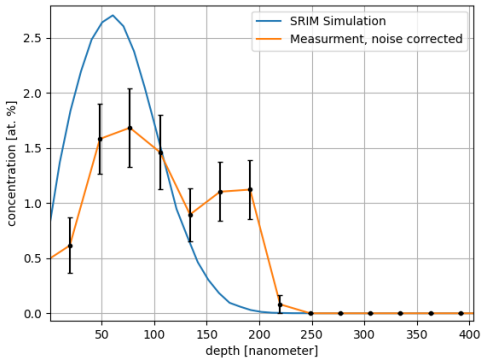

(c) UN_1_MIT, implanted with Zr

Figure 4.20: A comparison made between the SRIM simulation and ToF-ERDA measurements for samples UN_1_MIT, UN_2_MIT and UN-05 with error bars calculated through counting statistics.

In the SRIM simulation, 5% of the Kr ions, and 3.5% of the Zr ions backscatter when implanting into the UN matrix. Taking the backscattered ions into account, the theoretical implanted concentration was $9.22 \cdot 10^{15}$ atoms/cm^2 for Zr and $9.5 \cdot 10^{16}$ atoms/cm^2 for Kr. The theoretical implanted concentration was to be compared with the calculated implanted concentration. The results are shown in table 4.11.

Table 4.11: Theoretical implanted concentrations compared to calculated implanted concentrations for UN samples. Uncertainties are based on counting statistics.

Sample	Implanted Ion	TC [atoms/cm^2]	CC [atoms/cm^2]	Ratio (CC/TC)
UN-05	Kr	$9.5 \cdot 10^{16}$	$(4.52 \pm 0.15) \cdot 10^{16}$	0.47 ± 0.015
UN_1_MIT	Zr	$9.22 \cdot 10^{15}$	$(8.62 \pm 1) \cdot 10^{15}$	0.93 ± 0.11
UN_2_MIT	Kr	$9.5 \cdot 10^{16}$	$(4.51 \pm 0.19) \cdot 10^{16}$	0.47 ± 0.02

Table 4.11 shows the volatile nature of the noble gases implanted in the matrix since it is apparent that the implanted concentration of Kr is lower than what is predicted by SRIM. For the solid fission product, Zr, the implanted concentration was equal to what was expected.

A summary of the average concentration over the measured range is presented in Tables 4.12

through 4.15. Potku was used for statistical uncertainty analysis.

Table 4.12: UN-05

Element	Concentration [at. %]
U	19.61 ± 0.11
N	64.3 ± 0.4
O	10.8 ± 0.2
Kr	3.76 ± 0.1
C	1.07 ± 0.04

Table 4.13: UN-02

Element	Concentration [at. %]
U	22.9 ± 0.2
N	68.9 ± 0.8
O	6.1 ± 0.2
C	1.23± 0.09

Table 4.14: UN_1_MIT

Element	Concentration [at. %]
U	22.6 ± 0.2
N	68.4 ± 0.6
O	6.2 ± 0.2
Zr	1.13 ± 0.07

Table 4.15: UN_2˙MIT

Element	Concentration [at. %]
U	19.37 ± 0.14
N	65.1 ± 0.5
O	9.8 ± 0.2
Kr	3.83 ± 0.13

4.2.4 Post-implantation SEM and EDS measurements

The UN samples were, as said in Section 3.2, analyzed with SEM and EDS after implantation. The first sample analyzed was sample UN_ref_MIT. The line scan was made as shown in Figure 4.22.

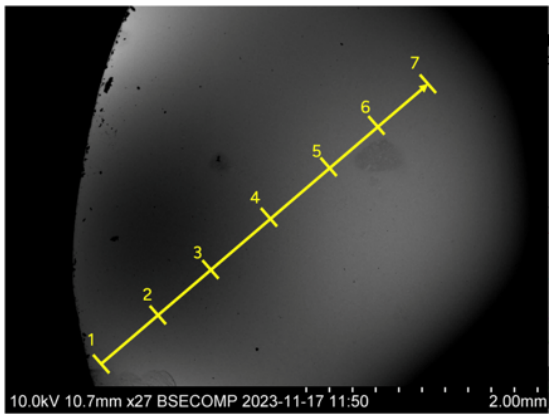

Figure 4.21: Image showing location of line scan.

Spectrum	N [%]	O [%]	Zr [%]	U [%]
1	26	21	5	48
2	29	18	2	51
3	31	18	0.8	52
4	32	15	0.3	54
5	32	13	0.2	55
6	32	12	0.2	56
7	33	10	0.1	57

Table 4.16: Concentrations in at. % of each spectrum in the line scan.

Figure 4.22: The results from SEM and EDS measurements of sample UN_ref_MIT.

By further analysis of Table 4.16, it can be seen that there was a clear gradient in the Zr implantation. It ranges from peak 5 at. % down to 0.1 at. % over the line scan. It can further be seen that there is a significant amount of O present near the surface and that the O seems to be dependant on the concentration of implanted species. The oxygen profile is consistent with the measurements made with ToF-ERDA in Figure 4.16.

Two more samples were analyzed with SEM and EDS as explained in Section 3.2. These were UN_1_MIT and UN_2_MIT. The analysis was made over the line separating the Kr and Zr implanted sides. The results from the EDS scan is shown in Figure 4.23.

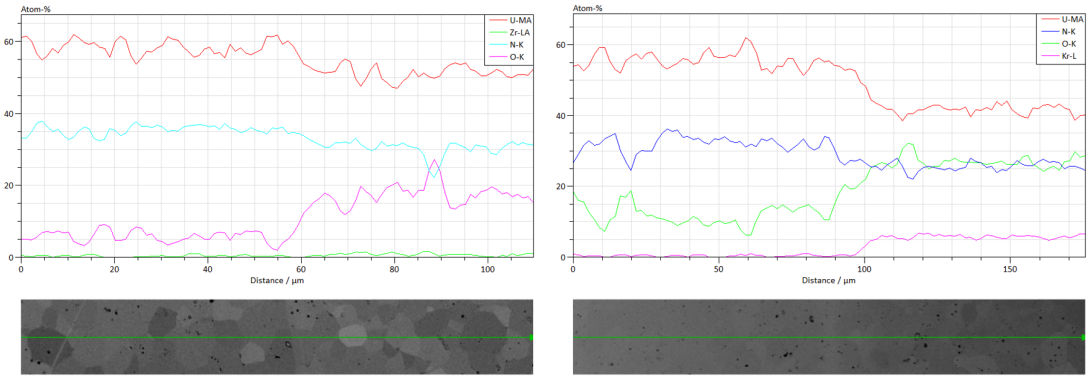

(a) EDS scan over implantation edge for UN_1_MIT

(b) EDS scan over implantation edge for UN_2_MIT

Figure 4.23: The results from the EDS scan performed on samples UN_1_MIT and UN_2_MIT.

The EDS scan showed that UN_1_MIT had an average of 1 at. % of Zr over the analysed area, and UN_2_MIT had an average of 7 at. % of Kr over the analyzed area. Figure 4.23 also further induces that the implantation seems to cause oxidation of the surface, since the concentration of O readily increases as the implanted species are introduced into the matrix. The mechanisms creating the oxide layer will be discussed in Section 5.2.

Chapter 5

Discussion

In this section, interpretations of the results obtained from the experiments will be presented. By comparing the findings with theoretical predictions and existing literature, the aim is to provide a comprehensive understanding of the underlying mechanisms present. Implications from the data presented and sources of errors will be discussed.

5.1 Diffusion study in ZrO_2

The ZrO_2 samples were implanted with Xe, Kr, and Fe and subsequently annealed at various temperatures and times. According to the predicted annealing concentrations shown in Figure 4.7, the concentration of Xe was expected to have a peak concentration of 23 at. % and Kr to have a peak concentration of 12 at. % after implantation and annealing. However, Figure 4.10 and Table 4.6 show a different outcome: the peak concentration of Xe was 0.5 at. % and Kr was 1.8 at. %. Since the annealed samples contained more Kr than Xe, it was deduced that Xe more easily escapes the ZrO_2 matrix.

The discrepancy might stem from the different levels of radiation damage induced in the samples. As explained in sections 2.3.1 and 2.5, different diffusion mechanisms dominate depending on the conditions for the sample. Figure 4.1 shows that the Xe implantation resulted in the highest level of induced damage. The increased damage likely explains the differences in the concentrations of Xe and Kr, since radiation-enhanced diffusion was probably more significant for the Xe implanted sample due to the greater amount of implanted damage. The damage induced can also explain the fact that less Xe was implanted than Kr, since during the implantation the sample is heated. The heating would then cause the sample to restore some of the implanted damage, and make it easier for the implanted species to escape the matrix. The effect will be especially strong for implantations of gaseous species, as explained in 2.3.1. The limited thermal diffusion visible in Figure 4.10, is attributed to the radiation-enhanced diffusion out of the surface. As seen in Figure 4.10, the shape of the concentration remains the same. The fact that the concentration profile does not alter in shape indicates further that the diffusion mechanism most dominant is not thermal diffusion. Moreover, it is interesting to note when comparing figure 4.7 and 4.10, that the simulations boundary conditions are inaccurate as the simulations in Figure 4.7 predict the implanted ions to accumulate near the surface. In reality, this is not the case. A better model of the boundary conditions is therefore needed to predict the diffusion of implanted ions better.

Figure 4.10c shows that no Iron was detectable with ToF-ERDA post-annealing. As explained in Section 3.5, an error was made in the simulation predicting the diffusion times. The error in the code made the prediction very inaccurate, and therefore the sample was annealed for far too long. For the subsequent annealings of ZrO_2-1, ZrO_2-2, and ZrO_2-3 the error in the code was fixed and therefore the predictions were more accurate. There could though, still be iron present

in the matrix, but on levels not detectible by ToF-ERDA. Measurements with more sensitive IBA techniques, such as PIXE, could be performed to evaluate if there still is some iron present.

Finally, the aluminium concentration present in some of the ZrO_2 samples needs to be addressed. As can be seen in figure 4.4, there was a concentration of Al in the samples that were implanted with Kr, and the concentration of Al concentration was also found in the post-annealing measurements, though then it was lower. A thorough analysis of the samples was made with SEM and ToF-ERDA, but no conclusion could be made as to where the aluminium concentration originated from. It was assumed that the aluminium content was introduced during the production of the ZrO_2 sticks.

In conclusion, the method of simulating the diffusion of implanted species in reactor fuel matrices by solving Fick's Second Law seems to work quite well as a first estimate. The prediction is not very accurate but works well enough to be able to predict annealing times to first order, meaning that it can predict for how long samples should be annealed to have measurable differences in the implanted distribution. Improvements could be made, especially in defining the physics and boundary conditions in the script. Surface physics and radiation-induced diffusion should be implemented, and more extensive measurements should be conducted.

5.2 Oxidation

During the implantations and subsequent ToF-ERDA measurements as well as EDS analysis, it was found that there was an oxide layer forming on the implanted UN samples as seen in Figure 4.16, Figure 4.19 and Figure 4.23. The reason for the forming of the oxide layer was assumed to be due to the heating and release of gases during implantation. As the sample heats during implantation, N is released as a diatomic gas as explained in 2.3.1. The release of N gas results in a U-rich surface being exposed to oxygen upon removal of the samples from the implantation chamber. Given that the samples were not allowed to cool after implantation, the high temperature of the samples likely caused oxidation when they came into contact with oxygen in the air when the chamber was opened.

5.3 Effects on the implanted UN matrix

Ion implantation affects the implanted sample matrix in different ways. Here the effect of the ion implantation on the UN matrix will be discussed through examples from the results. Since the implanted ions affect the lattice structure and create damage in the form of vacancies as well as taking up lattice sites that were initially occupied by U or N. To analyze the change in stoichiometry, the ratio of U to N was compared for implanted and unimplanted samples. To be able to compare the two quantities, the data from Potku was first normalized over the full range. This is shown in Figure 5.1.

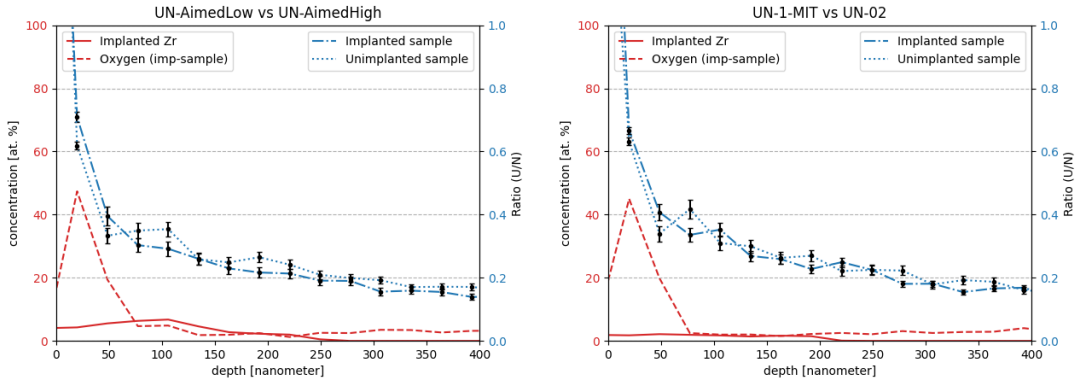

(a) Unimplanted and implanted spot for sample UN_ref_MIT

(b) Sample UN-02 compared with sample UN_1_MIT

Figure 5.1: The ratio of U to N in samples UN_ref_MIT and UN_1_MIT, both implanted with Zr. UN_ref_MIT was compared to an unimplanted spot on the sample, while UN_1_MIT was compared to UN02. The Zr implantation profile is shown in red.

In Figure 5.1, it can be seen that a higher concentration of implanted Zr seems to affect the sample matrix. It is apparent in Figure 5.1 that the ratio between U and N is lower in the implanted regions. The ratio is only different if there is a significant amount of implanted species present in the matrix, as seen by comparing Figure 5.1a and Figure 5.1b. Quantifying exactly how much the ratio changes will be hard due to the levels of noise present in the measurements.

To further see if there is a difference in the ratio of U to N, the same analysis was made for the Kr-implanted UN samples. The comparison is shown in Figure 5.2.

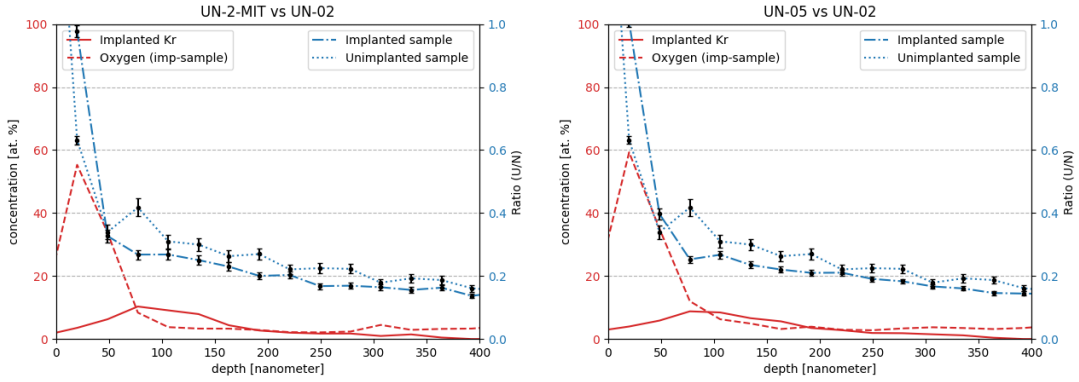

(a) Sample UN_2_MIT compared with sample UN-02

(b) Sample UN-05 compared with sample UN-02

Figure 5.2: The ratio of U to N in samples UN_2_MIT and UN-05, both implanted with Kr. Both samples UN_2_MIT and UN-05 were compared to UN02. The Kr implantation profile is shown in red.

In Figure 5.2, it is more noticeable that the ratio of U to N changes when implanting the sample with ions. As can be seen in Figure 5.2a and Figure 5.2b, the ratio between 50 nm to 200 nm is lower for the implanted sample. As the concentration of implanted species is reduced, so are the differences seen between the ratios. The ratio is greatly increased as the oxide layer forms.

The reason for the great increase in the ratio as the oxide layer forms is due to the decrease in N concentration. As outlined in Section 5.2, N gas is released, and then an oxide layer is formed on the N-depleted region. The reduction of N causes the ratio between U and N to greatly increase in the regions where the oxide layer is present, as the N concentration is reduced. The reduced ratio in the implanted regions, around 50 nm to 200 nm, is caused by the reduction of both U and N in these regions. The relative change in N is lower than the one in U, and therefore the ratio is reduced. The change in concentration of U and N is caused by displacements of the lattice by the implanted ions and causes a reduction of stoichiometry in the implanted UN matrices. Analysis with other IBA techniques such as RBS should be performed to further evaluate the effects of ion implantation on the UN matrix.

5.4 Comparison of predicted and actual implanted concentrations

In this section, the comparison of predicted and actual implanted concentrations will be assessed. In Tables 4.5 and 4.11 it can be seen that the predicted concentration profile is much higher than the actual concentration profile. SRIM predicts the implanted peak concentration to be higher than the measured peak concentration. The reason for the differences seen in implanted concentrations could be because of the stochastic behavior of ion implantation in combination with the heating that occurs when implanting. SRIM does not take into account any heating and might explain the differences seen. The heating may have caused the implanted ions to diffuse during the implantation and may have caused a broadening of the range in the samples. Therefore the ions reach further into the sample but do not have as sharp of a peak. The gas release caused by radiation-enhanced diffusion, as explained in Section 2.5, could also have caused the differences seen. There are also large levels of noise present in the measurements and the noise makes quantifying the ratio more challenging. Effects from backscattered ions and sputtering should also be addressed. As ions are implanted into a sample, some ions backscatter, and some ions sputter the surface. The backscattered ions were taken into account when calculating the concentrations in Tables 4.5 and 4.11. The sum of the effects presented above explains some of the differences seen in the implanted and measured concentrations.

It can be seen in Figures 4.7, 4.12 and 4.20, that the implanted concentrations of the solid ion, Zr and Fe, are in better agreement than that of the gaseous fission products, Xe and Kr. The reason that the difference in implanted and measured concentration is greater for the gaseous fission products is due to the volatile nature of the gaseous fission products. As explained in Section 2.5, the solubility of implanted ions in the sample matrix affects its stability. As Zr and Fe are more soluble than Xe and Kr, these will be more readily retained in the matrix. Xe and Kr can form gas bubbles, and induce more radiation damage which makes escaping the matrix easier.

5.5 Effects of heavy sample matrices

The use of a heavy sample matrix when performing measurements with ToF-ERDA gives rise to problems outlined in Section 2.6. These effects are pronounced in the measurements made on the heavy sample matrices like UN in this thesis. ToF-ERDA is optimized towards light elements and heavier elements struggle to reach the detectors due to their higher cross sections

and stopping powers as seen in equations (2.7) and (2.10). As the heavy elements have larger cross sections, most scatterings occur as forward scatterings of the ion beam. This is obvious in Figure 4.18, where most counts are on the forward scattered ion beam.

Heavy elements in ToF-ERDA suffer greatly from the effects of multiple and plural scattering. As the heavy elements have large cross sections, they scatter several times when traveling from inside the sample. The multiple- and plural scattering reduces the energy of these elements and causes the heavy elements to not reach the energy detector. The heavy elements can also scatter in random directions in the detector foils, and therefore not be detected. The absence of detection causes elements like U to have lower concentrations than expected in ToF-ERDA measurements. The low concentrations of heavy elements can be seen in all measurements made in this thesis on heavy elements like U. In Tables 4.7 through 4.10, it is evident that the average concentration of U in an implanted UN sample is around 20 at. % according to the measurement. The true concentration of U in UN is around 50 %.

The effect that heavy elements are harder to detect in ToF-ERDA measurements needs to be taken into account when drawing conclusions from the data. The concentration of U in the UN matrix is far greater than 20 at. %. To counteract the lower concentrations of heavy elements, a first order correction for the lower detection efficiency could be made by analyzing trends in the heavy element concentrations for different matrices. A comparative analysis between ToF-ERDA and methods that do not suffer from this effect could be made and from this correction factors could be derived. This was not done in this thesis.

Chapter 6

Conclusions and outlook

The proposed method by Frost et al. was used to study two different samples, ZrO_2 and UN. The project showed that the method works well to study the diffusion of both solid and gaseous fission products in heavy reactor fuel matrices. The method has been optimized and shows great promise for future studies conducted using the same method [1].

The study of diffusion of volatile fission products in the ZrO_2 matrix showed that to first order, annealing times can be predicted by solving Fick's second law (2.13) with numerical methods and SRIM simulations as input data. It was concluded that the method of ion implantation, analysis with ToF-ERDA, annealing, and re-analyzing with ToF-ERDA works well to study the behavior of gaseous fission products in heavy reactor fuel matrices.

In the UN matrix, the results showed that ion implantation reduces the ratio of Uranium to Nitrogen. It was concluded that the reduction was caused by the reduction of both U-atoms and N-atoms in the UN matrix, and since the relative change is lower for the N-atoms, the ratio is reduced. More data would though be needed to confirm that ion implantation affects the UN matrix in this way. It was also shown that the ratio between U to N greatly increases near the surface where the oxygen layer is formed. It was concluded that the increase is caused by the oxygen layer forming on the surface post-implantation.

During the thesis, the theoretically implanted concentrations were compared to the measured implanted concentrations. It was shown that the ratio between the measured implanted concentration to the theoretical implanted concentration was generally below one, and hence not all ions that were predicted to enter the sample matrix did. The discrepancy was caused by the volatile nature of inert gases implanted in the matrix. As they were implanted into the matrix, the gaseous fission products induced damage to the samples, which made escaping the matrix easier. For the solid fission products, there was still some release from the surface but it was not at all as apparent as it was for the gaseous fission products. It was concluded that there was a correlation between implanted damage and gas release during implantation, as the fission products that induced the most damage, also had the lowest measured implanted concentration.

Finally, it was shown that when heavy elements are present in ToF-ERDA measurements, the measurement shows that ToF-ERDA struggles in detecting these heavy elements. An attempt to derive first order correction factors has been made by Frost et al. [41].

6.1 Meeting of the project objectives

The key objectives of the project, outlined in Chapter 1, were met by implanting Xe and Kr in ZrO_2 and Zr and Kr in UN. The assessments of the implantations were made using ToF-ERDA, RBS, SEM, and XRD and the measurements were compared to theoretical data provided

by SRIM. Subsequently, sample annealing was performed at three different temperatures and annealing times on five out of the nine samples analyzed in the thesis. To assess the thermally-induced diffusion, ToF-ERDA was repeated on the samples and the measurements were analyzed and compared to each other. The script that solves Equation 2.13 was used to predict the annealing times, and its accuracy was evaluated the ToF-ERDA measurements. By performing the above-described steps, the project goals had been met.

6.2 Summary of key findings

The project resulted in several key findings, as deducted in Chapter 5. The most important findings were:

- The method proposed by Frost et al. works well for the study of diffusion of volatile fission products in heavy reactor fuel matrices as the concentrations of the implanted species can be assessed pre- and post-annealing [1].
- First order approximations of annealing times were derived through the use of Fick's second law with the diffusion coefficient modeled with Arrhenius Equation. The simulations were shown to be successful in predicting annealing times to first order.
- As ions are implanted into the UN matrix, the ratio of Uranium to Nitrogen is reduced.
- Ion implantation makes UN prone to oxidation as it is removed from the implantation chamber.
- The theoretical predictions of implanted concentrations did not correspond to the measured implanted concentrations. An attempt to quantify the ratio between the measured concentration and the theoretical concentration was made and showed that gaseous fission products generally had a lower ratio than solid fission products. This shows that it is more challenging to implant gaseous fission products.
- ToF-ERDA suffers from multiple- and plural scattering of heavy fuels present in the sample matrix. The multiple- and plural scattering events made quantifying the concentration of heavy elements challenging.

6.3 Suggestions for future work

In this section, we outline the potential directions for future research that could be conducted from the findings in this study. The conclusions drawn from the thesis open up more areas of research that need to be evaluated.

The method of predicting annealing times by solving Equation (2.13), needs to be evaluated more thoroughly with more samples to see if the output is continuously as correct as it was in this thesis. Implementations of more physics, such as radiation-induced diffusion, boundary conditions that account for surface physics, and more accurate diffusion coefficients need to be implemented.

The effects of ion implantation on heavy reactor fuels need to be studied more extensively to asses what mechanism causes the stoichiometry of the heavy fuels to alter during implantation. The oxidation mechanism also needs to be studied to a greater extent. Studies could be conducted by further implantation of elements into the UN matrix, and thereafter analyzing the stoichiometry and oxidation more thoroughly.

A more accurate method of estimating errors needs to be implemented when performing ToF-ERDA analysis with the 5 MV accelerator available at the Tandem laboratory at Uppsala University. This method needs to include the systematic errors that are present in the measurement by conducting extensive research on known reference samples and deriving correction factors.

Acknowledgements

First of all, I would like to express my deepest appreciation to my supervisor Dr. Robert Frost. I am extremely grateful for the support and insight he provided during the thesis, as well as his patience in teaching me how to run the equipment at the Tandem Laboratory. I would also like to express my gratitude to the people from KTH: Prof. Pär Olsson, Elina Charatsidou, and Maria Giamouridou. Thank you for all the help with questions that arose during the project, and all the lunches in the Q-Building. I would like to thank my subject reviewer, Prof. Daniel Primetzhofer, for taking his time to meet with me and suggest this project to me and for all the valuable feedback throughout the project. I also thank Dr. Mauricio Sortica, Johan Oscarsson, and Dr. Gyula Nagy, for providing extensive insight into the ion implantation processes and software used in the project. I would like to thank Emma and Lema for cheering me on during the project. Finally, I would like to thank Rebecca for all the time she spent listening to me ranting about physics during this semester.

Appendix

A Uncertainty analysis

The uncertainty analysis in Potku was conducted by subtracting the noise from the measurement. Particles hitting a detector is a Poisson distributed quantity. This means that the standard deviation is defined as

$$\sigma = \sqrt{n}, \tag{A.1}$$

where n is the number of counts in an event. In the software used, Potku, the total number of counts per element measured is displayed so this can be used to conduct uncertainty analysis.

Let S be the true number of counts in the measurement, M be the number of counts measured for one element in Potku and N be the number of background counts. The true number of counts is then equal to

$$S = M - N, \tag{A.2}$$

where S, M and N is defined as above. Thereafter, the uncertainty for the signal, S, can be calculated by propagating the error from M and N as

$$\sigma_{tot} = \sqrt{\sqrt{M}^2 + \sqrt{N}^2} = \sqrt{M + N}. \tag{A.3}$$

From equation (A.3), the relative uncertainty can be calculated as

$$\sigma_{REL} = \frac{\sqrt{M + N}}{M - N}. \tag{A.4}$$

The calculated relative uncertainty, σ_{REL}, was then multiplied by the calculated implanted concentration to achieve the uncertainties presented in Tables 4.5 and 4.11. To achieve the error bars in Figures 4.17 and 4.20 the error analysis was performed binwise.

B SIMNRA Spectra

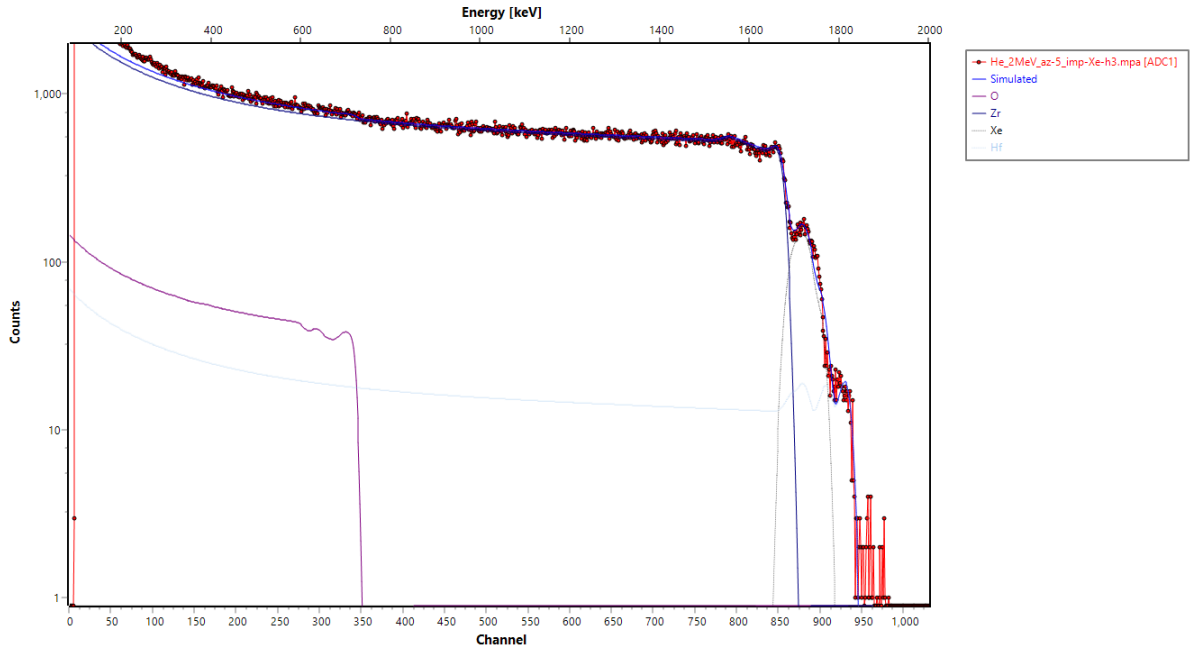

Figure B.1: Fitted SIMNRA spectrum of sample ZrO_2-2.

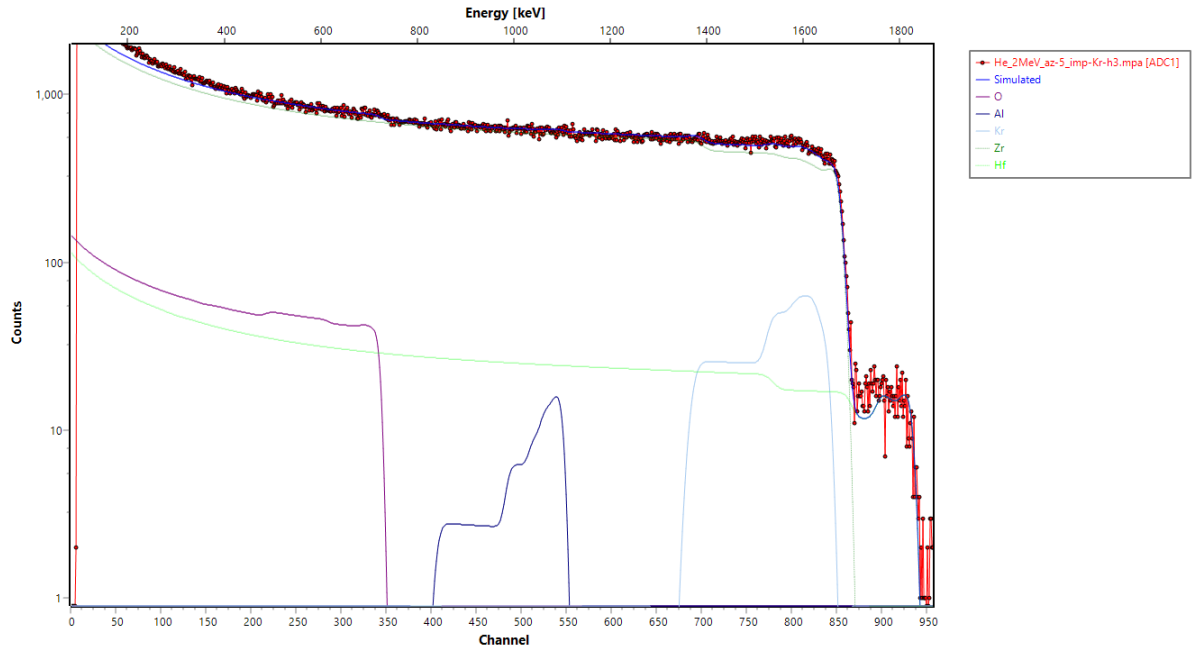

Figure B.2: Fitted SIMNRA spectrum of sample ZrO_2-3.

References

[1] R. Frost, D. Lopes, K. Johnson, *et al.* Evaluating the diffusion of Kr in UO2 and ADOPT^{TM} using Time-of-Flight Elastic Recoil Detection Analysis (ToF-ERDA). *Journal of Nuclear Science and Technology* (2024)

[2] C. Friskney, M. Speight. A calculation on the in-pile diffusional release of fission products forming a general decay chain. *Journal of Nuclear Materials*, vol. 62 (1976), 89–94. doi:https://doi.org/10.1016/0022-3115(76)90286-5

[3] I. A. E. Agency. Fission Product Release Mechanisms and Groupings. *IAEA Bulletin* (1994)

[4] M. Natasi, J. Mayer. Dynamics of Binary Elastic Collisions, In *Ion implantation and synthesis of Materials*, chap. 3. Springer (2006)

[5] F. Priolo. *Fundamentals of surface film analysis: Atomic collisions and backscatter spectrometry*. International Centre for Theoretical Physics (1994)

[6] K. Gärtner. Ion-Solid Interaction, In *Ion Beam Modification of Solids*, chap. 1. Springer (2006)

[7] C. Lindon. *The Encyclopedia of Spectroscopy and Spectrometry*. Oliver Walter (2000)

[8] M. Natasi, J. Mayer. Radiation damage, In *Ion implantation and synthesis of Materials*, chap. 5. Springer (2006)

[9] J. F. Ziegler, J. P. Biersack. The Stopping and Range of Ions in Matter, In D. A. Bromley, ed., *Treatise on Heavy-Ion Science, Volume 6: Astrophysics, Chemistry, and Condensed Matter*, 95–128. Springer Science+Business Media, New York (1985). ISBN 978-1-4615-8105-5. doi:10.1007/978-1-4615-8103-1_3

[10] B. Gu, D. Munñoz Santiburcio, F. Da Pieve, *et al.* Bragg's additivity rule and core and bond model studied by real-time TDDFT electronic stopping simulations: The case of water vapor. *Radiation Physics and Chemistry*, vol. 193 (2022), 109961. doi:10.1016/j.radphyschem.2022.109961

[11] J. Ziegler, M. Ziegler, J. Biersack. SRIM – The stopping and range of ions in matter (2010). *Nucl. Instrum. Methods Phys. Res. B*, vol. 268 (2010), 1818–1823. doi:10.1016/j.nimb.2010.02.091

[12] M. Natasi, J. Mayer. Radiation damage, In *Ion implantation and synthesis of Materials*, chap. 7. Springer (2006)

[13] H. Matzke. Radiation damage in nuclear materials. *Nuclear Instruments and Methods in Physics Research Section B: Beam Interactions with Materials and Atoms*, vol. 65 (1992), 30–39. doi:https://doi.org/10.1016/0168-583X(92)95010-O

[14] J. Turnbull, C. Friskney, J. Findlay, F. Johnson, A. Walter. The diffusion coefficients of gaseous and volatile species during the irradiation of uranium dioxide. *Journal of Nuclear Materials*, vol. 107 (1982), 168–184. doi:https://doi.org/10.1016/0022-3115(82)90419-6

[15] M. Gerardin, E. Gilabert, D. Horlait, M.-F. Barthe, G. Carlot. Experimental study of the diffusion of Xe and Kr implanted at low concentrations in UO2 and determination of their trapping mechanisms. *Journal of Nuclear Materials*, vol. 556 (2021), 153174. doi:https://doi.org/10.1016/j.jnucmat.2021.153174

[16] B. Eyre, R. Bullough. The formation and behaviour of gas bubbles in a non-uniform temperature environment. *Journal of Nuclear Materials*, vol. 26 (1968), 249–266. doi:https://doi.org/10.1016/0022-3115(68)90099-8

[17] J. Rest, M. Cooper, J. Spino, *et al.* Fission gas release from UO2 nuclear fuel: A review. *Journal of Nuclear Materials*, vol. 513 (2019), 310–345. doi:https://doi.org/10.1016/j.jnucmat.2018.08.019

[18] M. Natasi, J. Mayer. *Ion implantation and synthesis of Materials*. Springer (2006)

[19] W. Wesch, E. Wendler. *Ion Beam Modification of Solids*. Springer (2016)

[20] H. Ryssel. *Ion implantation techniques*. Springer (1982)

[21] J. Pelleg. Diffusion in Ceramics, chap. 1. Springer International Publishing (2016). doi:10.1007/978-3-319-18437-1_1

[22] P. Van Uffelen, M. Suzuki. 3.19 - Oxide Fuel Performance Modeling and Simulations, In R. J. Konings, ed., *Comprehensive Nuclear Materials*, 535–577. Elsevier, Oxford (2012). ISBN 978-0-08-056033-5. doi:https://doi.org/10.1016/B978-0-08-056033-5.00071-9

[23] G. Murch. Ferrite and Austenite: Diffusion, Bulk and Interfacial, In K. J. Buschow, R. W. Cahn, M. C. Flemings, *et al.*, eds., *Encyclopedia of Materials: Science and Technology*, 3009–3012. Elsevier, Oxford (2001). ISBN 978-0-08-043152-9. doi:https://doi.org/10.1016/B0-08-043152-6/00536-2

[24] H. Matvke. Diffusion processes in nuclear fuels. *Journal of the Less Common Metals*, vol. 121 (1986), 537–564. doi:https://doi.org/10.1016/0022-5088(86)90573-4

[25] P. C. T. D'Ajello, C. Scherer. Radiation enhanced diffusion in solid bilayers. *Journal of Physics D: Applied Physics*, vol. 25 (1992), 1713. doi:10.1088/0022-3727/25/12/014

[26] H. Matzke. Atomic mechanisms of mass transport in ceramic nuclear fuel materials. *J. Chem. Soc., Faraday Trans.*, vol. 86 (1990), 1243–1256. doi:10.1039/FT9908601243

[27] Dependence of Diffusion on Temperature and Pressure, 127–149, In *Diffusion in Solids: Fundamentals, Methods, Materials, Diffusion-Controlled Processes*. Springer Berlin Heidelberg, Berlin, Heidelberg (2007). doi:10.1007/978-3-540-71488-0_8

[28] F. Adams, C. Barbante. Chapter 8 - Particle-Based Imaging Techniques, In F. Adams, C. Barbante, eds., *Chemical Imaging Analysis*, vol. 69 of *Comprehensive Analytical Chemistry*, 315–337. Elsevier (2015). doi:https://doi.org/10.1016/B978-0-444-63439-9.00008-6

[29] W. Assmann, H. Huber, C. Steinhausen, *et al.* Elastic recoil detection analysis with heavy ions. *Nuclear Instruments and Methods in Physics Research Section B: Beam Interactions with Materials and Atoms*, vol. 89 (1994), 131–139. doi:https://doi.org/10.1016/0168-583X(94)95159-4

[30] S. Giangrandi, K. Arstila, B. Brijs, *et al.* Considerations about multiple and plural scattering in heavy-ion low-energy ERDA. *Nucl. Instrum. Methods Phys. Res. B*, vol. 267 (2009), 1936–1941. doi:10.1016/j.nimb.2009.03.105

[31] K. Arstila, J. Julin, M. Laitinen, *et al.* Potku – New analysis software for heavy ion elastic recoil detection analysis. *Nucl. Instrum. Methods Phys. Res. B*, vol. 331 (2014), 34–41. doi:10.1016/j.nimb.2014.02.016

[32] M. Janson. CONTES conversion of time-energy spectra – A program for ERDA data analysis. User manual, Uppsala University, 2004

[33] B. Doyle, D. Brice. The analysis of elastic recoil detection data. *Nucl. Instrum. Methods Phys. Res. B*, vol. 35 (1988), 301–308. doi:10.1016/0168-583X(88)90286-8

[34] JEOL. *SEM Scanning Electron Microscope A to Z: Basic Knowledge for Using the SEM.*

[35] S. J. Reed. Introduction to Energy Dispersive X-ray Spectrometry (EDS) (1995). URL `https://cfamm.ucr.edu/media/126/download`. Accessed: 2024-05-28

[36] N. E. Widjonarko. Introduction to Advanced X-ray Diffraction Techniques for Polymeric Thin Films (2016)

[37] E. Charatsidou, M. Giamouridou, A. Fazi, *et al.* Proton irradiation-induced cracking and microstructural defects in UN and (U,Zr)N composite fuels. *Journal of Materiomics*, vol. 10 (2024), 906–918. doi:https://doi.org/10.1016/j.jmat.2024.01.014

[38] M. Mayer. *SIMNRA User's Guide*. Max-Planck-Institut für Plasmaphysik, Garching bei München, Germany (1997). Report IPP 9/113

[39] M. Gérardin, E. Gilabert, D. Horlait, M.-F. Barthe, G. Carlot. Diffusion of Xe and Kr implanted at low concentrations in UO2 as a function of temperature – An experimental study. *Journal of Nuclear Materials*, vol. 582 (2023), 154476. doi:https://doi.org/10.1016/j.jnucmat.2023.154476

[40] A. Dragoo. Diffusion Rates in Inorganic Nuclear Materials. *Journal of research of the National Bureau of Standards* (1968), 157–173. doi:10.1016/j.nimb.2019.04.024

[41] R. Frost, D. Primetzhofer, E. Ntemou, *et al.* Elemental depth-profiles of very-heavy sample matrices measured by ToF-ERDA (2024)